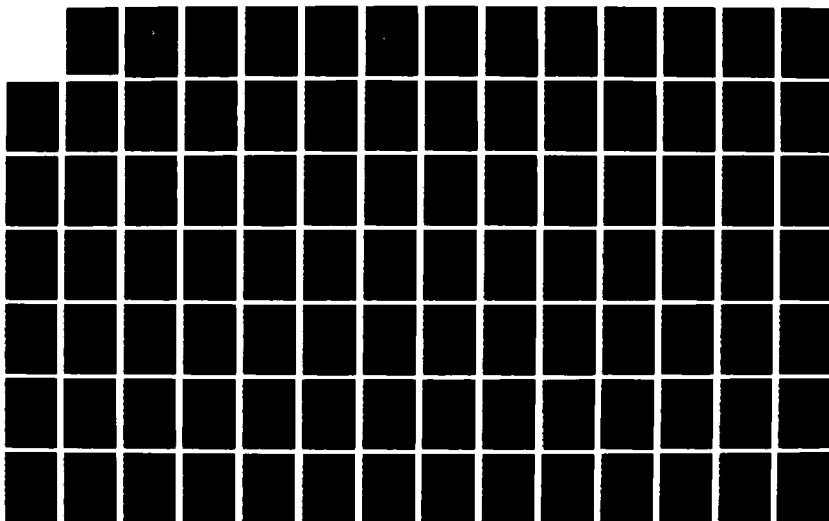GEOPHYSICAL INVESTIGATIONS AT PAHUTE MESA NEVADA(U)
TEXAS UNIV AT DALLAS RICHARDSON J F FERGUSON ET AL
12 AUG 87 AFGL-TR-87-0242 F19628-85-K-0028

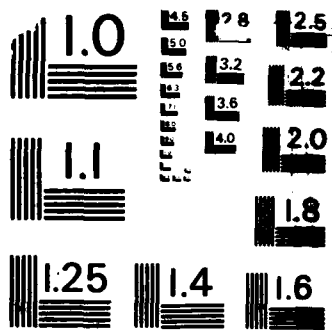UNCLASSIFIED

F/G 8/7

NL

MICROCOPY RESOLUTION TEST CHART
NATIONAL BUREAU OF STANDARDS–1963–A

AFGL-TR-87-0242

Geophysical Investigations at Pahute Mesa, Nevada

John F. Ferguson
Sharon K. Reamer

University of Texas at Dallas
P.O. Box 930688
Richardson, Texas 75083

AD-A190 478

DTIC
ELECTED
JAN 1 2 1988
D

12 August 1987

Final Report
1 February 1985-31 January 1987

88 1 5 010

REPORT DOCUMENTATION PAGE

Form Approved
OMB No. 0704-0188

1a. REPORT SECURITY CLASSIFICATION	1b. RESTRICTIVE MARKINGS
Unclassified	AD-A190478

2a. SECURITY CLASSIFICATION AUTHORITY	3. DISTRIBUTION/AVAILABILITY OF REPORT
	Approved for Public Release. Distribution
2b. DECLASSIFICATION/DOWNGRADING SCHEDULE	unlimited.

4. PERFORMING ORGANIZATION REPORT NUMBER(S)	5. MONITORING ORGANIZATION REPORT NUMBER(S)
	AFGL-TR-87-0242

6a. NAME OF PERFORMING ORGANIZATION	6b. OFFICE SYMBOL (If applicable)	7a. NAME OF MONITORING ORGANIZATION
University of Texas at Dallas		Air Force Geophysics Laboratory

6c. ADDRESS (City, State, and ZIP Code)	7b. ADDRESS (City, State, and ZIP Code)
P.O. Box 830688	Hanscom AFB
Richardson, TX 75083	Massachusetts 01731-5000

8a. NAME OF FUNDING/SPONSORING ORGANIZATION	8b. OFFICE SYMBOL (If applicable)	9. PROCUREMENT INSTRUMENT IDENTIFICATION NUMBER
Defense Advanced Research Projects Agency	NMRO	F19628-85-K-0020

8c. ADDRESS (City, State, and ZIP Code)	10. SOURCE OF FUNDING NUMBERS			
1400 Wilson Boulevard	PROGRAM ELEMENT NO	PROJECT NO.	TASK NO	WORK UNIT ACCESSION NO
Arlington, VA 22209-2308	61101F	5A10	DA	AN

11. TITLE (Include Security Classification)

(U)Geophysical Investigations at Pahute Mesa, Nevada

12. PERSONAL AUTHOR(S)
John F. Ferguson, Sharon K. Reamer

13a. TYPE OF REPORT	13b. TIME COVERED	14. DATE OF REPORT (Year, Month, Day)	15. PAGE COUNT
Final Report	FROM 2/1/85 TO 1/31/87	1987 August 12	128

16. SUPPLEMENTARY NOTATION

17. COSATI CODES			18. SUBJECT TERMS (Continue on reverse if necessary and identify by block number)
FIELD	GROUP	SUB-GROUP	underground nuclear explosions, Pahute Mesa, NV, geologic
			structure, gravity modeling; seismic exploration at NTS

19. ABSTRACT (Continue on reverse if necessary and identify by block number)

The seismic response of nuclear tests at Pahute Mesa, NV, displays variations which correlates with the geologic/geophysical structure. Investigations have been performed using borehole, gravity and wide angle seismic observations, with the aim of producing a geophysical model of the Silent Canyon caldera structure at Pahute Mesa. Empirical models of the density and seismic velocity have been formulated based on well logs. New gravity stations were obtained in 1985 and merged with older, lower quality data. A new gravity modeling technique was developed and applied to the modeling of a transect across the area. The resulting model supports the hypothesis that a high density and velocity "basement" composed of Silent Canyon caldera rocks underlie a lower density and velocity blanket at a depth of a few kilometers. In 1986 a wide angle seismic reflection/refraction survey was completed near the gravity profile. The 15 km long line crossed the buried caldera boundary as well as important normal faults. The shot point was located on outcropping basement. Future interpretation of the combined gravity and seismic data should permit the construction of a predictive geophysical model.

20. DISTRIBUTION/AVAILABILITY OF ABSTRACT	21. ABSTRACT SECURITY CLASSIFICATION
☒ UNCLASSIFIED/UNLIMITED ☐ SAME AS RPT. ☐ DTIC USERS	Unclassified

22a. NAME OF RESPONSIBLE INDIVIDUAL	22b. TELEPHONE (Include Area Code)	22c. OFFICE SYMBOL
JAMES LEWKOWICZ	(617)377-3028	AFGL/LWH

DD Form 1473, JUN 86   Previous editions are obsolete.   SECURITY CLASSIFICATION OF THIS PAGE

Unclassified

Table of Contents

iii

Introduction

Recent seismological investigations of nuclear tests at the Nevada Test Site (NTS) have manifested the need for multidimensional geophysical models of the shallow (less than 5 km) structure. Careful analysis of seismic signals has established a pattern of response variations both at Yucca Flat and Pahute Mesa. These variations include both amplitude and travel time perturbations (Alewine, personal communication, Minster et al., 1981 and Taylor, 1983) and may also be azimuth dependent (Lynnes and Lay, 1984).

The body wave magnitude anomalies observed by Alewine are plotted in Figure 1 along with the Bouguer gravity anomaly. The gravity anomaly appears to reflect the structure of the 14 my old Silent Canyon caldera collapse feature, which is now buried beneath younger volcanics (locally to over 2 km depth). The body wave magnitude anomaly correlates rather well with the gravity feature, which strongly suggests a common explanation for the seismic response anomaly in terms of the Silent Canyon caldera structure. This hypothesis is best approached by the construction of a structural model using geologic and geophysical data which are largely independent of the nuclear tests themselves. A reliable model of this type can be used to test the seismic

1

Figure 1. The body wave magnitude anomaly is plotted on a map of the Bouguer gravity for Pahute Mesa, Nevada.
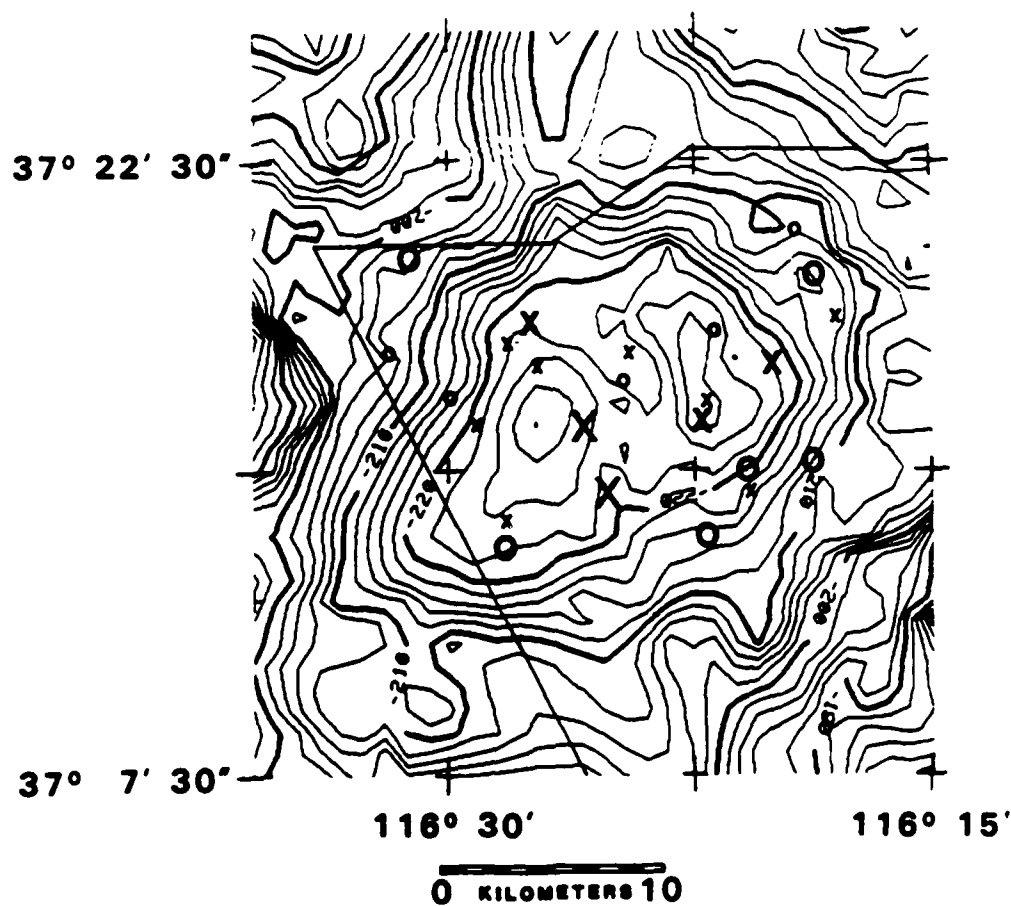
BOUGUER GRAVITY 2 mgal CONTOURS

Δmb

O   ≥ 0.2
OO   0.1 = 0.2
o   0.0 - 0.1
x   −0.1 - 0.0
X   −0.2 - −0.1
X   ≤ −0.2

2

response to confirm or reject the hypothesis. Ferguson (1987) applies this approach to Yucca Flat with some success. It is important to explain as much of the variation as possible with known (i.e. independently determinable) features of the crust and then relegate the remaining, reduced variation to less accessible explanations.

Two-dimensional structural models can be treated by a number of techniques, such as finite differences (Kelley et al., 1976), the Aki-Larner method (Aki and Larner, 1970) and generalized ray theory (Helmberger et al., 1985) to name a few examples. These methods are being applied to NTS structures (McLaughlin et al., 1987 and Ferguson, 1987), particularly at Yucca Flat where the structure is fairly simple and better known (Ferguson et al., 1988). Techniques applicable to three-dimensional models may be practical in the near future.

In order to meet the new requirements for geophysical modeling at Pahute Mesa, we have attempted to gather pertinent geologic and geophysical data and produce a consistent interpretation of these data in terms of geophysical profiles. The use of wide angle seismic surveys at Pahute Mesa is an innovation which is being tested as a part of this study. The approach taken here is to make use of geologic mapping and borehole explorations to a full extent. Borehole geophysics is

useful in the calibration of geologic models for geophysical purposes. Density and velocity measurements made in boreholes have been assembled and analyzed. Gravity observations permit a uniform areal coverage where boreholes are limited and are often a good indication of seismically important structures. Gravity data are availible at NTS and new data are inexpensive to obtain. Seismic reflection and refraction have not been used in Pahute Mesa investigations previously due to several mitigating factors. A novel approach to the seismic survey has been attempted, but it remains to be seen whether or not the data will be sufficiently sensitive to the lateral structure variations at Pahute Mesa.

Geologic Background

The geology of the Pahute Mesa has been the subject of numerous publications since the publication of Nevada Test Site, Memoir 110 of the Geological Society of America (Eckel, 1968). Important papers in that volume include Noble et al. (1968) and Orkild et al. (1968) which identify and describe the Silent Canyon caldera. Ten years of geologic mapping on 7 1/2 minute quadrangles was complied at a scale of 1:48000 by Orkild et al. (1969) on the Geologic Map of Pahute Mesa, Nevada Test Site and Vicinity, Nye County, Nevada. Radiometric age dates were published by Kistler (1968) and Marvin et al. (1970). Papers on the Timber Mountain and related calderas to the south were included in Memoir 110 and were also published in the 1970's (Byers et al., 1976 and Christiansen et al., 1977). Exploration for nuclear waste isolation sites to the south of Timber Mountain and continued drilling in support of the testing program at Pahute Mesa have encouraged a more recent synthesis of the geologic data by Warren et al. (1985). Large scale geophysical structure of the test site has been pursued by Minster et al. (1981), Taylor (1983) and Hoffman and Mooney, (1984). This sample of literature is not exhaustive,

but is sufficient to support the overview of the geologic history to be presented here.

The southwestern Nevada volcanic field extends from Goldfield, Nevada southeast to Mercury, Nevada. A number of major volcanic centers occur along a north-south trend along the western boundary of NTS. Silent Canyon caldera is north of the most persistent center(s) at Timber Mountain and is almost totally buried under younger volcanics at Pahute Mesa (Figure 2).

The geologic history is summarized in Table 1. The volcanism of the southwest Nevada volcanic field begins about 15 or 16 my ago with eruptions from undefined centers and some material (the Rhyolite of Kawich Valley) from Silent Canyon caldera. These older volcanics overlie Paleozoic clastic and/or carbonate rocks and possible granitic rocks similar to the Climax and Gold Meadows plutons at Pahute Mesa. The volcanism may be related to the occurence of north-south trending normal faults. About 14 my ago the Silent Canyon caldera collapsed producing the Belted Range tuff. These units are unusual in that they are peralkaline in composition rather than the more common calc-alkaline of the older and younger volcanics. We hypothesize that the Belted Range tuff and stratigraphically equivalent lavas form the geophysical basement under Pahute Mesa.

6

Figure 2. The major volcanic centers of the southwestern Nevada volcanic field are shown with an outline of the Nevada Test Site for reference.
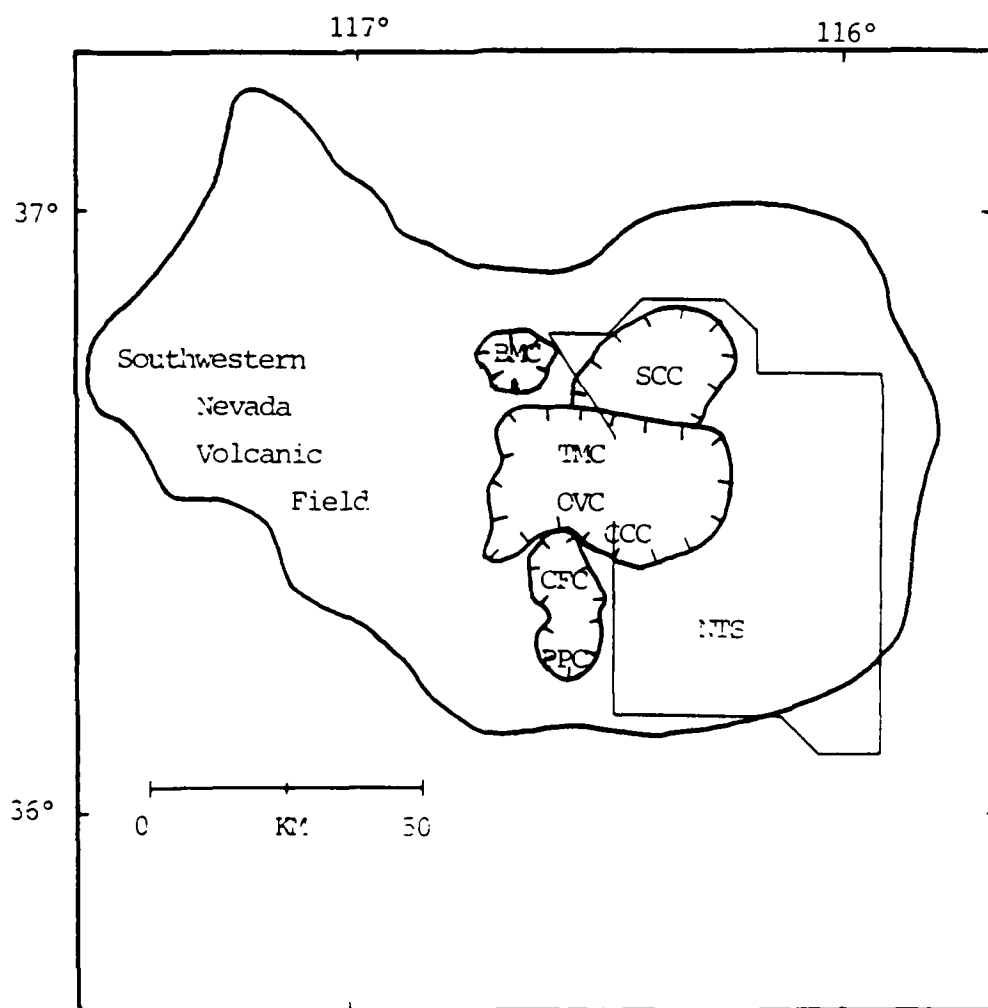

7

Table 1

Period	Lithology	Description
Late Quaternary	Alluvium	Ranging from a thin veneer to hundreds of meters in the grabens
	Basalt lavas (Buckboard Mesa)	Locally, small amounts
Early Quaternary /Late Tertiary		Basin and range graben development on NS faults with EW extension and late developing strike-slip with N50W extension
Late Tertiary K-Ar ages[*]		
9.5-6.2 my	(Thirsty Canyon)	Black Mt. caldera
11-10.4 my	(Timber Mt)	Timber Mt. caldera collapse
		NE trending faults with N78W extension
13-12 my	(Paintbrush)	Claim Canyon calderon NW trending faults
13.2-12.4 my	calc-alkaline (Area 20)	Silent Canyon caldera subsidence, more peralkaline on the east side
		NS faults inactive
13.5-14 my	calc-alkaline (Crater Flat)	Crater Flat caldera
13.8 my	peralkaline (Belted Range)	Silent Canyon caldera collapse
		Normal faulting on NS trend
16-14 my	(Redrock Valley) (Fraction) (Tunnel Beds) (Rhyolite of Kawich Valley)	Local volcanic centers Silent Canyon caldera
27 my	Intermediate volcanics (Monotony Valley)	Wide-spread volcanism on a NE trend NTS to Utah
Early Tertiary		High-angle faulting NW trend (?)
Late Cretateous	Granitic intrusives (Climax stock)	
Middle to early Mesozoic	No sedimentation	Orogeny
Permian to Pennsylvanian	Carbonates	Stable margin (12 km total thickness pC to now)
Mississippian to late Devonian	Clastics from Roberts Mt. thrust	Orogeny
Early Devonian to late Cambrian	Carbonates	Stable margin
Early Cambrian to late Precambrian	Clastics	Stable margin

[*] K-Ar ages from Kistler (1968) and Marvin et al. (1970)

The younger Tuffs and Lavas of Area 20 were erupted into Silent Canyon caldera about 13 my ago and the caldera was filled by Paintbrush tuff from Claim Canyon cauldron, on the south side of Timber Mountain, between 13 and 12 my ago.

The collapse of Timber Mountain caldera produced the Timber Mountain tuff, including the vitrophyre of the Rainer Mesa member, which caps the by now filled in Silent Canyon structure. Note that the area to the southeast of Pahute Mesa, although now a topographic low, must have been structurally high throughout most of this time. Belted Range rocks are now exposed there. The exact nature of the structure between the Silent Canyon and Timber Mountain calderas is also not well known. A small amount of Thirsty Canyon tuff from the Black Mountain center to the west is found locally at Pahute Mesa. Both northwest and north-south trending faults have been active at Pahute Mesa during the Tertiary and northeast trending faults have been important regionally. During the Paintbrush deposition, the northwest trending Silent Canyon shear zone was active in northern Pahute Mesa, truncating the north-south faults and bounding the low lying depositional area. The Split Ridge, Scrugham Peak, Almendro, West Greeley, East and West Boxcar and Purse north-south

9

trending faults have been significant throughout the caldera history (Figure 3).

The caldera collapse entailed a more or less elliptical zone of faulting or slumping as indicated on the map of Orkild et al. (1969) and in Figure 3. The margin is not well exposed and the boundary shown is interpretive in nature. Geophysical investigations may help to clarify the margin structure and the configuration of the post-Belted Range Silent Canyon caldera structure.

Figure 3. Map of the major structural features of Pahute Mesa, Nevada.

MAJOR STRUCTURES AT PAHUTE MESA, NV
SCALE 1: 288000

11
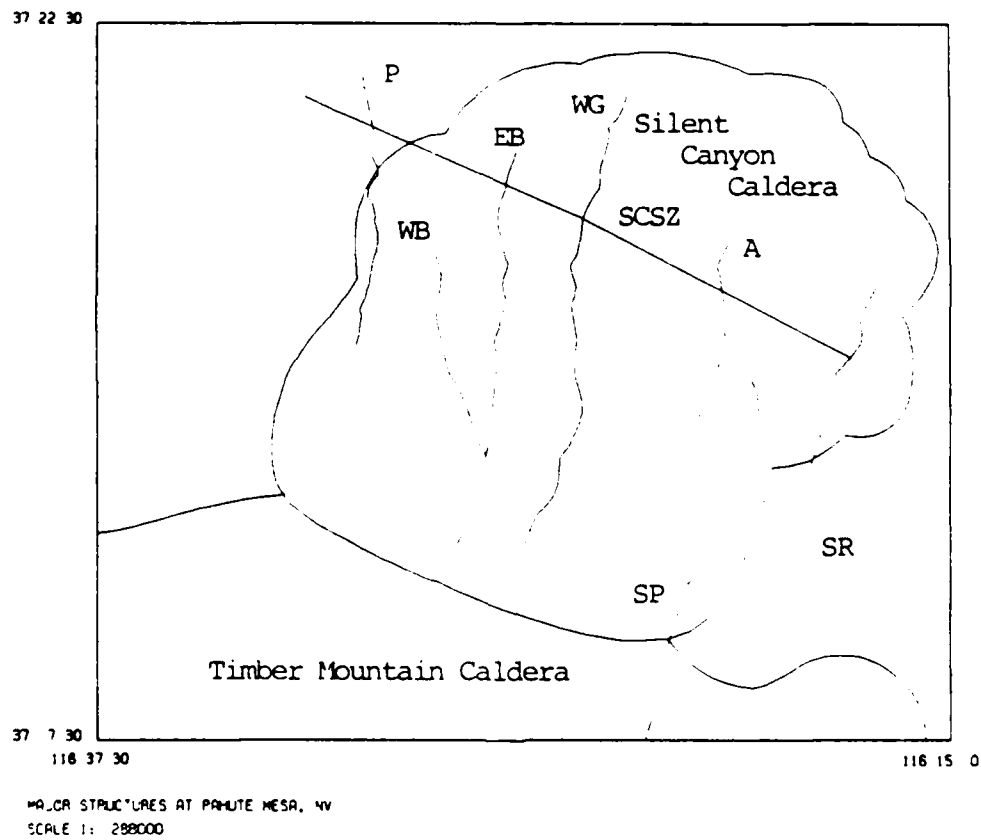
Analysis of Geophysical Logs

Borehole geophysical logs are routinely made at NTS in exploratory and emplacement holes for containment studies. In this investigation borehole gravity, density logs and borehole velocity surveys have been of particular interest. Well logs from 23 holes were obtained from the GEODES data base at Los Alamos. The log availablity is summarized in Table 2. Only two wells in the western half of the Mesa were studied and the depth extent is generally limited to less than 700 m. Where deep (1 to 2 km) holes exist, only density information is available. The important holes used in this investigation are plotted on Figure 4.

Several goals were identified: 1) Can geophysically distinct geologic units be identified ? 2) Can the geologic/geophysical units be characterized by simple, well defined velocity and density functions ? 3) Can a relationship be found between velocity and density so that velocity can be predicted from the more abundant density data ?

It should be pointed out that this study has been hampered by a lack of good stratigraphic logs for these holes. Some of the older logs are in error and positive identification of some of the units is difficult at best. Recent studies by Richard Warren at Los Alamos using

12

Table 2

Well	Density	Gravity	Velocity	Water Level	Depth Extent
U19aa	*		*	709	600
U19af	*	*	*	695	
U19ae	*	*	*	707	700
U19ak		*	*	655	600
U19ab	*	*	*		700
U19x	*	*	*	715	700
Ue19z		*	*	668	800
U20n		*		625	1200
PM-1		*		644	2200
Ue20f		*			1300
U19ad		*			700
Ue19n		*			400
U19x		*			700
Ue19p1	*				700
U19g	*	*		627	700-1000
U19ar	*				700
Ue19p	*			690	600
Ue19gs	*				1300-2300
Ue19fs1	*				800-1400
Ue19i	*				900
Ue19x	*				800
Ue19g	*			627	700-900

*   indicates that the log is available.

All depths are in meters.

13

Figure 4.   Locations of wells used in this study for stratigraphic control and geophysical log analysis.

BOREHOLES WITH GEOPHYSICAL LOGS AT PAHUTE MESA, NV
SCALE 1: 288000
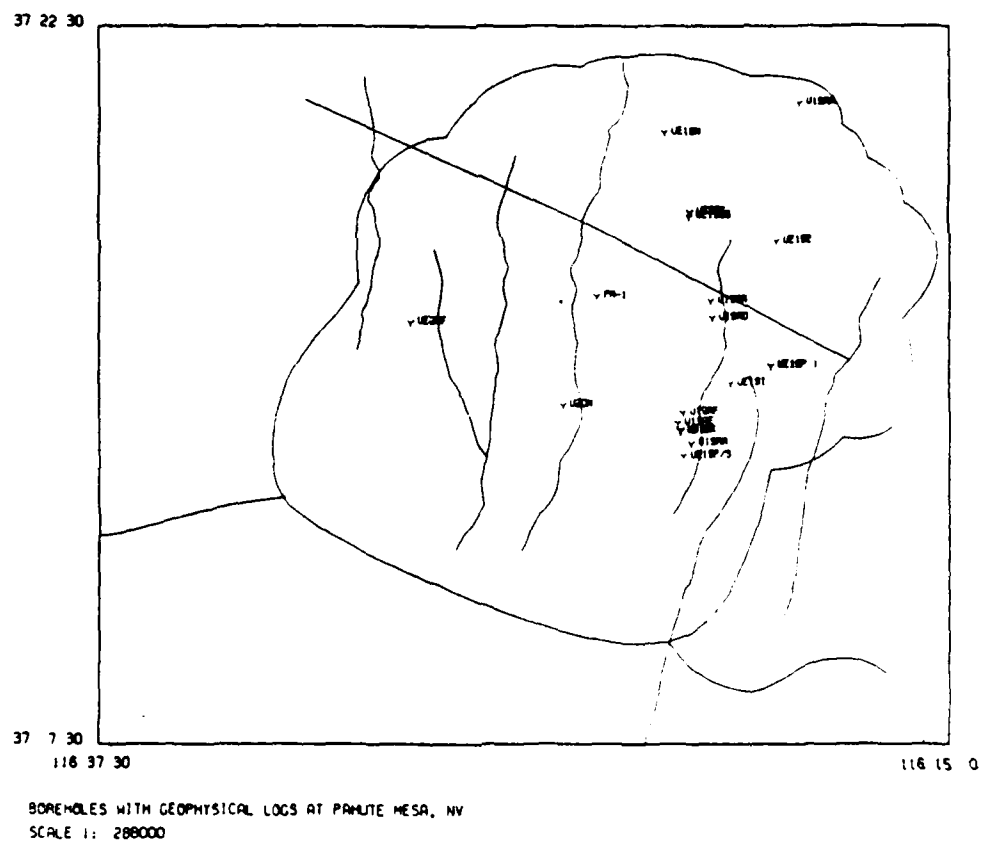
geochemical and petrologic techniques have helped to eleviate this problem, but the work is as yet incomplete.

Initially the borehole gravity in the deepest holes, like PM-1 and Ue20f, were analyzed to obtain a density function for the caldera filling tuff units. The function

$$\sigma(z) = 1750 + 420 \, z, \quad (km, \, kg/m^3)$$

was fit to PM-1. Exceptions to this relation are higher density lava units and the Belted Range tuff (Tbt) which is associated with what we term the pre-caldera basement. The Tbt appears to have a density near 2500 kg/m^3. This model was found to predict the tuff densities below 0.5 or 0.6 km in other borehole gravity logs. The model and the density data for PM-1 and Ue20f are shown in Figure 5. Borehole gravity is a very good way to characterize bulk density due to its sensitivity to a volume of rock around the borehole, for the same reason it can also be subject to bias if significant structures are nearby (Hearst and Carlson, 1982).

The holes containing both density and velocity data were analyzed in greater detail, particularly U19af, U19ae, U19x and U19ab which are near the seismic line. The more distant holes Ue19z and u19ak were also studied. Geophysical data for these holes were grouped according to rock type by intervals. These groups were Rainer Mesa tuff (Tmr), all other tuffs and lavas. Zeroth and first degree polynomial models were fit to the data for each

15

Figure 5. Densities computed from borehole gravity in wells PM-1 and Ue20f. The density function derived from PM-1 below 600 m is shown along with the density profiles.

$$\rho(z) = 1750 + 420z$$
ρ in kg/m^3, z in km
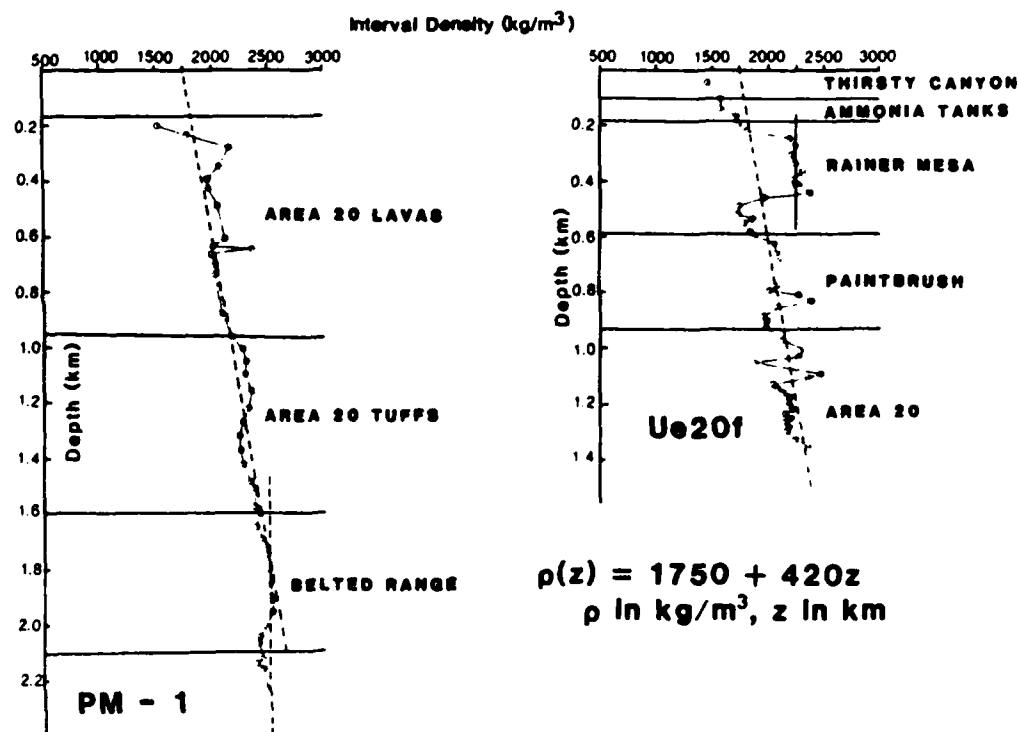
hole by group and for all holes combined by group by least squares. It should be noted that the use of least squares for this purpose is probably not appropriate, but the results seem to be consistent. The models based on the data combined from all six holes are summarized below:

Velocity (km and km/sec):

Tuffs (including Tmr) -

$v(z) = 1.70 + 2.15\ z$

Lavas -

$v(z) = 2.9$

Density (km and kg/m^3) :

Tuffs (excluding Tmr) -

$\sigma(z) = 1510 + 740\ z$

Lavas and Tmr -

$\sigma(z) = 2200$

The root mean square error for the velocity models is 0.7 to 1.0 km/sec and 100 to 120 kg/m^3 for the density models. The correlation coefficient is an acceptable 0.8 for the tuff density model and a rather poor 0.5 for the tuff velocity model. The models are plotted along with logs for U19af and Ue19z in Figure 6. The lavas are not a well defined geophysical unit. The lava intervals are somewhat indistinct and the physical properties are highly variable. They do show a tendency to a higher density, but the velocity is not well distingished from

17

Figure 6. Density and P-wave velocity profiles from U19af and Ue19z. The shallow velocity and density models are also plotted.
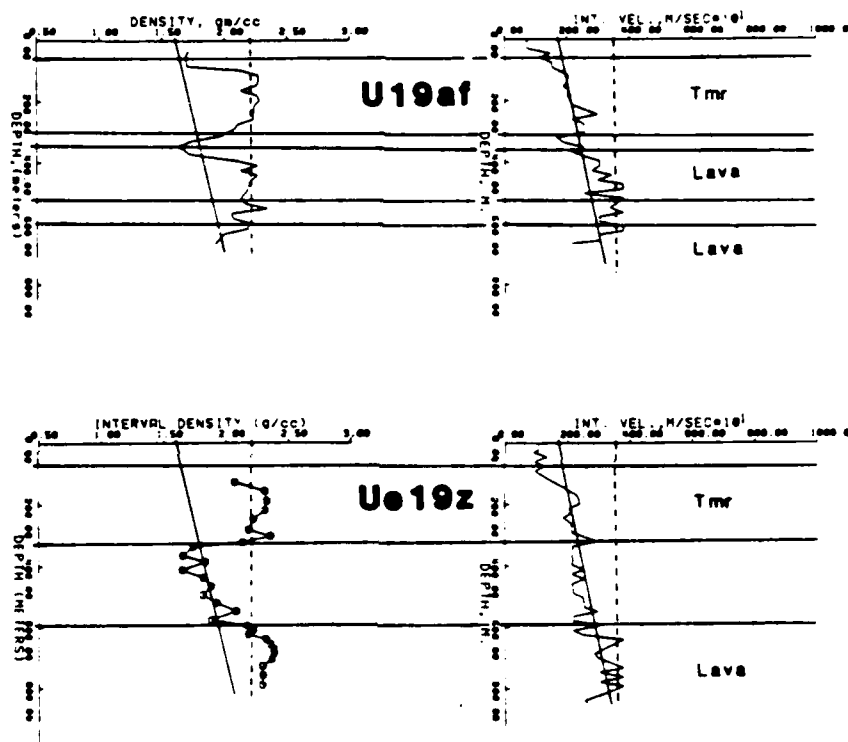
Velocity:
Tuffs–
$$v(z) = 1.70 + 2.15\ z\ \ km/sec$$
Lavas–
$$v(z) = 3.50\ \ km/sec$$

z in km

Density:
Tuffs (excluding Tmr)–
$$\rho(z) = 1.51 + 0.74\ z\ \ gm/cm^3$$
**Lavas and Tmr–**
$$\rho(z) = 2.20\ \ gm/cm^3$$

PAHUTE MESA GEOPHYSICAL LOGS

18

the tuffs. The lava velocity distribution is better characterized by a large variance and a broad, almost uniform probability distribution. If the lavas were to be grouped with the tuffs the result would be effected only slightly. The Rainer Mesa tuff is similar in velocity structure to the other tuffs and is definitely of a higher density.

The velocity and density models developed for these six holes are all based on data acquired above the water table, which occurs at about 0.65 to 0.7 km. The density model developed for PM-1 is valid only below depths of 0.6 km. It is significant that the intercept density is greater and the gradient is lower for the deep model. Some implications of this will be discussed in a later paragraph. A similar effect should also occur in the velocity vs. depth function. A velocity model recently published by Leonard and Johnson (1987) supports this conclusion. Their model is displayed in Figure 7 along with the tuff velocity model developed here and the raw interval velocities for tuff and lava intervals. The linear polynomial model is biased slightly low, but the gradient is similar down to 0.6 km depth. The Leonard and Johnson model was found by a linearized inversion of the travel times from nuclear tests out to offsets of 12 km. The model represents a gross vertical and horizontal average of the true velocity distribution. The tremendous

19

Figure 7. The shallow velocity model from this report, the Leonard and Johnson velocity profile and the raw interval velocities from Area 19 holes are plotted together on this figure for comparison.

VELOCITY (KM/SEC)

- TUFFS
- LAVAS
- - - - FERGUSON (1986)
—— LEONARD AND JOHNSON (1987)
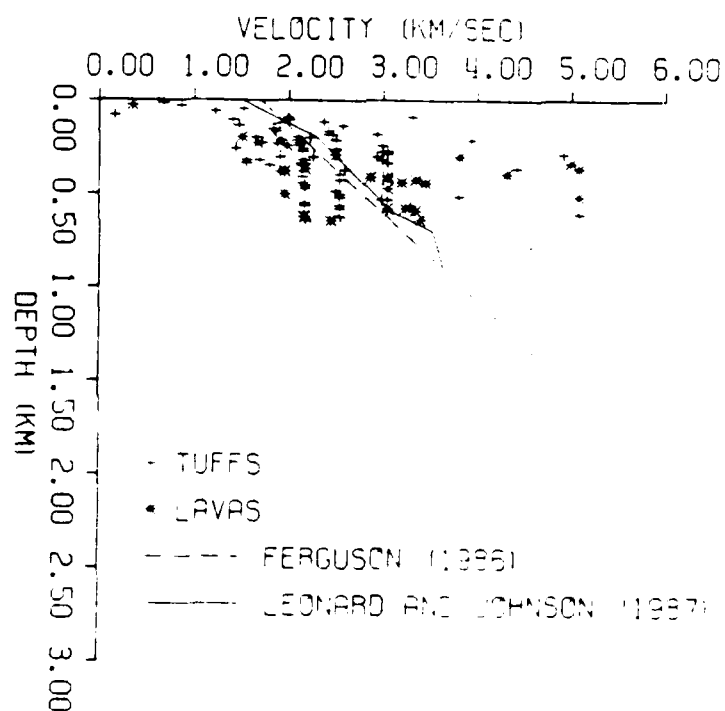
scatter of the the measured interval velocities about these average models should be noted. At a depth of 2 km the velocity approaches 4.6 km/sec and the travel time data lose resolution. A clear break in the velocity gradient is observed in the vicinity of the water table. The deeper velocities are predicted by

$$v(z) = 3.1 + 0.6 \ z \ km/sec.$$

Geophysically, zones of wet and dry tuff are distingished on the basis of property gradient with depth.

The density and also the velocity of clastic sedimentary rocks depend greatly on the porosity and these volcanic rocks might also be expected to display this effect. The tuffs are initially very porous (30 % or more) and the porosity decreases with depth due to compaction. The compaction and porosity are also strongly effected by secondary mineralization, glassiness of the matrix and welding. The lavas could have a great range of properties from vugginess to very low porosity. We can make some speculations based on a theoretical compaction model for sedimentary rocks (Korvin, 1984). The porosity should obey an exponential law of the form

$$\phi = \phi_0 \ \exp(-kz) \ .$$

If k is small this might be reasonably replaced by a linear relationship, such as

$$\phi = \phi_0 - kz \ .$$

Given a simple mixing law for the density

21

$$\sigma = \phi\, \sigma_f + (1 - \phi)\sigma_m \; ,$$

we can obtain the linear density function

$$\sigma(z) = \sigma_m - \phi_0(\sigma_m - \sigma_f) + k(\sigma_m - \sigma_f)z \; .$$

If we assume that the porosity decrease rate, k, and the matrix density, σ_m, are constant and that the only difference in the shallow and deep density functions is the pore fluid density, σ_f, we can conclude that $k = 0.28$ or 0.29, for air in the shallow pores and water in the deeper pores. The difference in the intercept values for the density models is less well explained by this hypothesis, as a discrepancy of 160 kg/m^3 occurs. The surface porosity, ϕ_0, is found to be 40 %, which is reasonable for these tuffs.

The velocity models are much more difficult to reconcile with the porosity. Published empirical relationships (Gardner, et al., 1974) between porosity and velocity,

$$v = \phi \, / \, v_f + (1 - \phi) \, / \, v_m \; ,$$

and density and velocity,

$$\sigma = a \, v^{0.25} \; ,$$

are inconsistent and neither seems to fit the density or porosity functions estimated from the density data. It was expected that the shallow and deep velocity functions could be explained by a simple change in pore fluid similar to the density relationships, but this has not been realized. The empirical relationship in Ibrahim and

22

Keller (1981) for volcanic rocks does not fit these data and it is difficult to tell if the rocks studied in that paper are at all similar to those at Pahute Mesa. Due to this problem a predictive relationship between density and velocity has not been established and a different approach will be taken in the future. The availability of the Leonard and Johnson velocity model makes the prediction of velocity from density less crucial to the geophysical modeling effort.

Gravity Modeling Technique

Fourier Gravity Inversion Technique:

The gravity modeling technique to be applied at Pahute Mesa must be capable of using the linear density function indicated by the log analysis. Although initially two-dimensional models will be considered, Three-dimensional calculations should be possible. Ferguson et al. (1988) have demonstrated that the so called Parker-Oldenburg technique (Parker, 1972 Oldenburg, 1974) is effective in the inversion of large, three-dimensional problems. In this report an extension of the original formulation to include a linear density function will be made. Although no three-dimensional calculations will be made here, the extension from two to three dimensions is not difficult.

Parker (1972) formulated the forward potential field calculation by assuming the source of the gravitational anomaly to be a layer at some depth, z_0, bounded by variable interface topography $h(\underline{r})$ and $g(\underline{r})$, and density contrast $\sigma(\underline{r})$ (Figure 8). Depth, z, is taken to be positive downward. Starting with the Fourier transform of the gravitational potential given by :

$$F[U(r_0) = G\ \sigma \int_X \int_D \int_{g(\underline{r})}^{h(\underline{r})} \exp(i\ \underline{k}\cdot\underline{r})\ /\ |r_0-r|\ dz\ dS\ dS_0 \quad ,$$

r_0 = position of the observation

24

Figure 8. Schematic description of parameterization of
the Fourier gravity inversion technique as derived by
Parker (1972) and Oldenburg (1974). Note that in this
description, z is positive downward and σ is a function
of lateral position.
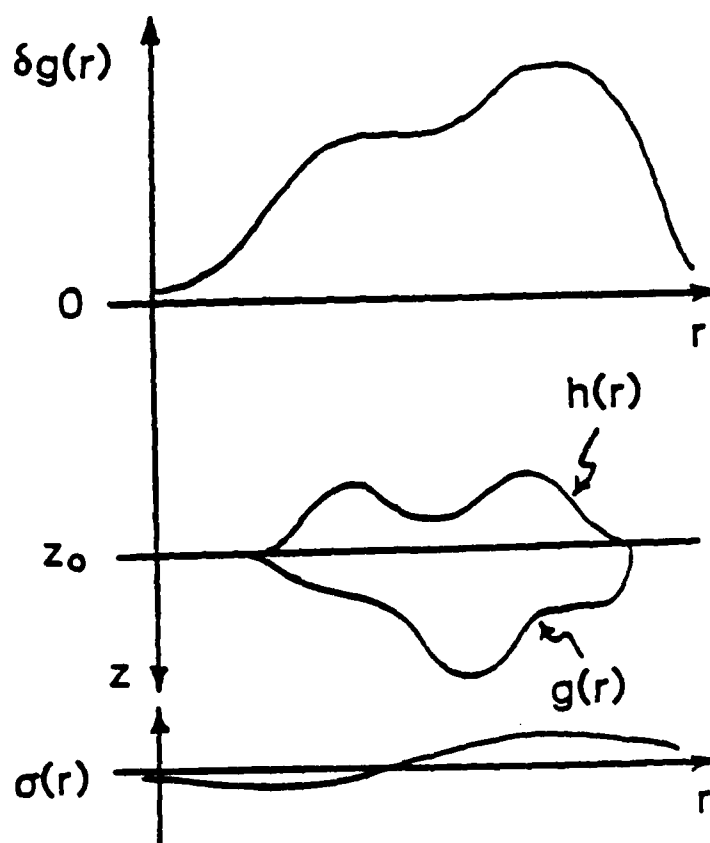
r = position within the volume to be integrated

$\underline{r}$ = projection of r onto the surface $z = 0$

and integrating over domains X and z, the resulting integral becomes:

$$F[U(r_0)] = 2\pi\ G\ \sigma \int \exp(i\ \underline{k}\cdot\underline{r} - |\underline{k}|z_0)$$

$$\cdot\ \{\ \exp(|\underline{k}|\ (h(\underline{r}) - g(\underline{r})))\ \}\ /\ |\underline{k}|^2\ \ dS$$

After a Taylor series expansion of the exponential function of the interface topography, $\exp[h(\underline{r})-g(\underline{r})]$,

$$F[U(r_0)] = 2\pi\ G\ \sigma\ \exp(-|\underline{k}|z_0)\ \cdot\ \sum_{n=1}^{\infty} |\underline{k}|^{n-2}\ /\ n!$$

$$\cdot\ F[h^n(\underline{r}) - g^n(\underline{r})]$$

the integral then becomes a Fourier transform of sums of successive powers of the interface topography. Differentiating this expression yields the equation for the gravity effect:

$$F[\delta g(\underline{r})] = 2\pi\ G\ \sigma\ \exp(-|\underline{k}|z_0)\ \cdot\ \sum_{n=1}^{\infty} |\underline{k}|^{n-1}\ /\ n!$$

$$\cdot\ F[h^n(\underline{r}) - g^n(\underline{r})]$$

Oldenburg (1974) derived the inverse solution by solving for the first order source topography term, $[h(\underline{r})-g(\underline{r})]$. This results in the inverse solution by the method of successive approximations:

$$F[h(\underline{r}) - g(\underline{r})] = -F[\delta g(\underline{r})]\ \exp(|\underline{k}|z_0)\ /\ (2\pi\ G\ \sigma)$$

26

$$\cdot \sum_{n=2}^{\infty} |\underline{k}|^{n-1} / n! \ F[h^n(\underline{r}) - g^n(\underline{r})]$$

The derivation by Parker (1972) and Oldenburg (1974) could be formulated with a laterally varying density function, $\sigma(\underline{r})$:

$$F[\sigma(\underline{r}) \ (h(\underline{r}) - g(\underline{r}))] = -F[\delta g(\underline{r})] \ \exp(|\underline{k}|z_0) / (2\pi \ G \ \sigma)$$

$$\cdot \sum_{n=2}^{\infty} |\underline{k}|^{n-1} / n! \ F[\sigma(\underline{r}) \ (h^n(\underline{r}) - g^n(\underline{r}))] \ .$$

This result is a non-linear inverse solution for parameterization of a depth model using potential field data. As discussed by Oldenburg (1974), parameterization of this model is non-unique. A _priori_ specification of the density distribution and one of the bounding surfaces reduces some ambiguity of this non-uniqueness.

Addition of a Vertically Varying Density Function:

Since density is a function of depth within the Earth, it is useful to derive the Fourier transform of the gravity effect with a vertically varying density function. Assume that $\sigma(z)$ is a linear function such that

$$\sigma(z) = \sigma_0 + cz \ ,$$

where σ_0 is the density contrast on the observation plane and c is the density gradient. Replacing σ in the forward calculation with $\sigma(z)$ results in the following expression for the two-dimensional case,

27

$$F[\delta g(\underline{r})] = 2\pi \, G \, \exp(-|\underline{k}|z_0) \, \{ \, \sigma_0 \sum_{n=1}^{\infty} |\underline{k}|^{n-2} / n!$$

$$\cdot \, F[h^n(\underline{r}) - g^n(\underline{r})] + c \sum_{n=2}^{\infty} |\underline{k}|^{n-1} / n!$$

$$\cdot \, F[h^n(\underline{r}) - g^n(\underline{r})]$$

where z is taken to be positive downward. The inverse expression then becomes:

$$F[h(\underline{r}) - g(\underline{r})] = F[\delta g(\underline{r})] \, \exp(|\underline{k}|z_0) / (2\pi \, G \, \sigma)$$

$$- \sum_{n=2}^{\infty} \{ \, |\underline{k}|^{n-1} / n! + (c/\sigma_0) \, |\underline{k}|^{n-2} / n! \, (n-1) \, \}$$

$$\cdot \, F[h^n(\underline{r}) - g^n(\underline{r})]$$

A detailed derivation of this result is given in the Appendix. Note that instead of summation over one infinite series, this result contains two infinite series. The first series is essentially the same as that in the original results of Parker (1972) and Oldenburg (1974). The second series, which adds the effects of the vertical density gradient, has no apparent effect on the first order interface term, which is the largest term, since series summation begins at n = 2. The effect of a density gradient on the first infinite series becomes apparent by considering the effect of shifting the observation plane, z_0 , as suggested by Parker (1972) to speed convergence of the solution. For the constant density case this shifting does not affect the magnitude

28

of the resulting gravitational anomaly. In the case of the vertical density function, if the z_0 plane is shifted, the initial density, σ_0, must also be shifted. Magnitude of the gravity effect in the forward solution and model depth in the inverse solution are then scaled as a result of the density gradient.

Since each series is summed separately, the convergence of each series should be tested separately. Tests for convergence of the Taylor series, as discussed by Parker (1972) are applied. Convergence of the inverse solution is also controlled by the stability of the explicit downward continuation function, $\exp(|\underline{k}|z_0)$.

Shallow source regions and observational error cause the continuation function to increase rapidly with increasing depth and force the inverse solution to diverge. Low pass filtering of the data suppresses this effect. However, eliminating short wavelength effects with an arbitrary low pass filter results in overfiltering or underfiltering of the data introducing greater misfit between observed and theoretical gravity data (Ferguson et al., 1988). In addition, if the bandwidth of the filter is too large, the inclusion of high wavenumber information will still result in divergence of the inverse solution.

A better method of stabilization of the downward continuation process can be achieved by application of a

regularization function as described by Tikhonov et al. (1968):

$$f(\underline{k}, \alpha, z) = 1 \; / \; (1 + \alpha^2 \; \underline{k}^2 \; \exp(|\underline{k}|z))$$

The effect of this filter is to taper the downward continuation function before it begins to grow large. For low wavenumber values, the filter has a minimal effect (Figure 9). As the wavenumber increases, the exponential function begins to decay rather than grow. The amount of tapering is controlled by the parameter α. As shown in Figure 9, application of the filter with a large α value rapidly tapers the exponential function whereas a more gradual taper is achieved with smaller α. Optimizing the regularization filter consists of finding an optimal value for α which controls the growth of the downward continuation without tapering too rapidly. Ferguson et al. (1988) used the Nelder-Mead polytope technique (1965) to search the solution space for the α value which best minimized the root mean square (rms) error between observed and calculated gravity anomaly values after each iteration of the inversion. A limitation of this method is that a reasonable first approximation for α is required to insure rapid convergence of the Nelder-Mead simplex technique. Also, computational efficiency of the Fourier gravity inversion technique is decreased because of additional evaluations

Figure 9. Amplitude of the downward continuation function increases exponentially with increasing wavenumber. Regularization tapers the exponential growth with the amount of tapering proportional to the value of the filter parameter α. This figure illustrates the effect of increasing α values on downward continuation.


31
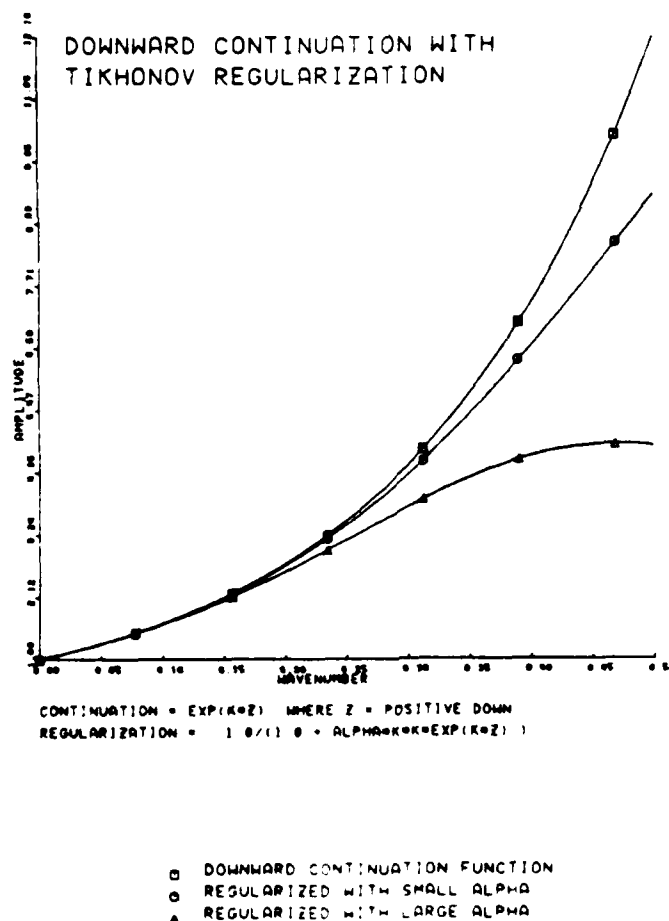
of the forward solution used in the search for an optimal value for α.

Characteristics of Potential Field Spectra:

To optimize of the regularization filter, spectral characteristics of potential field data are considered. Spector and Grant (1970) and Hahn et al. (1975) demonstrated that potential field spectra have a characteristic shape which is dominated by the effect of source depth. The effect of source depth produces a linear relationship between the logarithmic power spectrum and wavenumber, the slope of the line being proportional to the source depth (Figure 10). A power spectrum of gravity anomaly data produced by sources at multiple depths can be characterized by a series of line segments with different slopes.

Shallower sources have correspondingly lower spectral slopes. Observational errors, if statistically uncorrelated to the data, are represented by "white noise," the mean spectral value of which is a constant or flat line. As is shown in Figure 10, the effects of deeper sources dominate the low wavenumber portion of the spectrum, whereas shallower sources and white noise dominate the higher wavenumbers. In this study, the gravity effect of deeper sources is considered to be the anomaly of interest; therefore, the portion of the spectrum represented by deeper sources is assumed to be

32

Figure 10. Graphical representation of potiental field spectra. Part (a) illustrates a spectrum with sources at three different depths, z_1, z_2, and z_3. Slopes of line segements representing each depth are proportional to the depth with steepness of slope indicating greater depth. Noise is indicated by the flat part of the spectrum. Part (b) illustrates the assumption used in the regularization process; a single source at depth z produces the observed gravity effects and is considered the signal (dominating the low wavenumbers) and is distinct from noise which has a flat spectrum (dominates higher wavenumbers). Crossover wavenumber separates signal from noise and occurs when the ratio of signal to noise equals one.
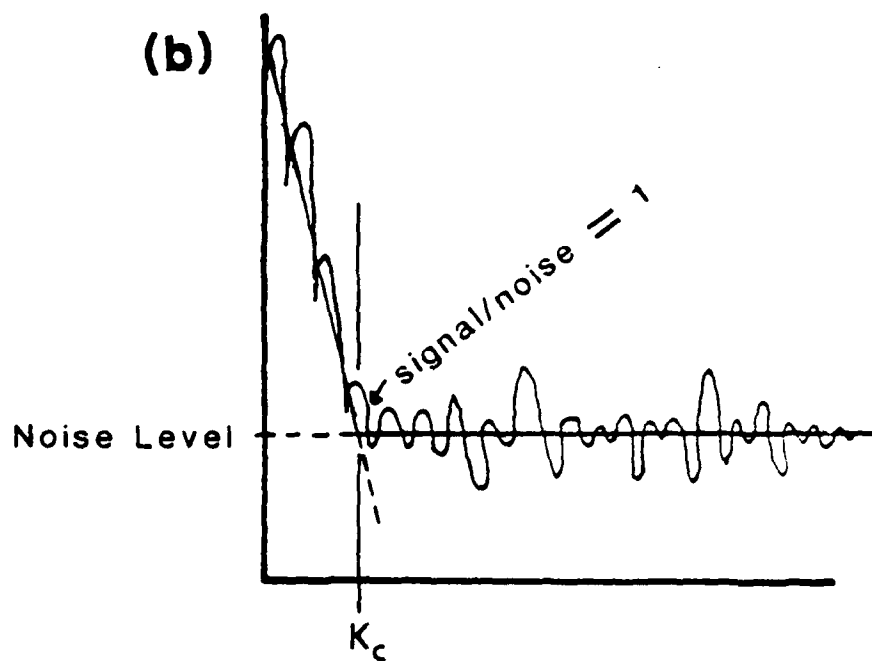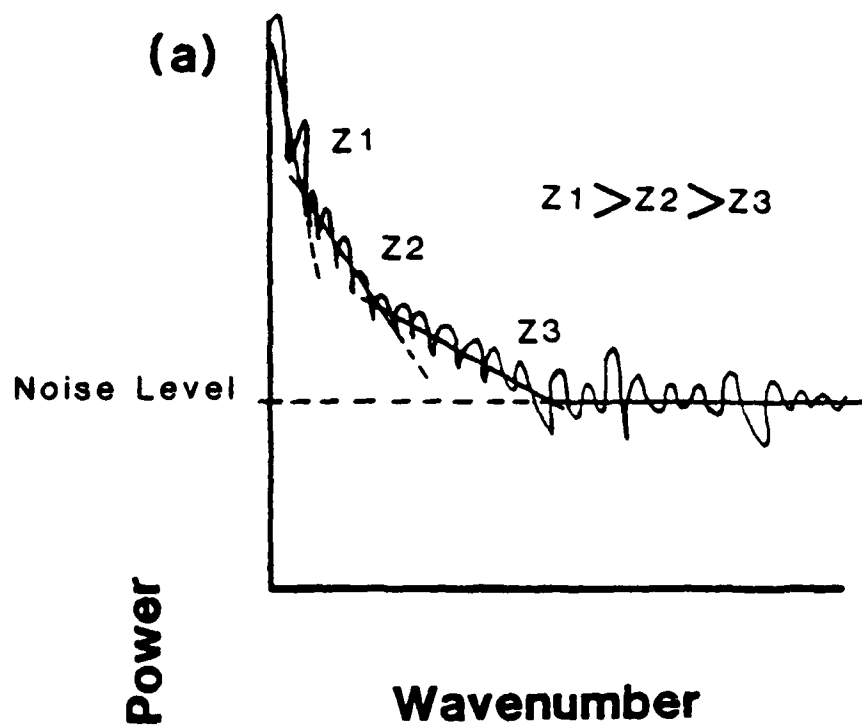
the signal. Other portions of the spectrum representing shallow sources or fluctuations due to observational error are considered undesirable components of the overall gravity effect and are assumed to be noise.

Since amplitude or power of the signal decays linearly for potential field data plotted on a semi-logarithmic scale, the effect of noise begins to dominate as the slope of the signal falls below the noise level. The point at which the signal/noise ratio equals unity, termed the crossover wavenumber (k_c), is the wavenumber after which the effect of noise dominates the spectrum (Figure 10).

In order to regularize the downward continuation function without overfiltering or underfiltering the data, is necessary to choose the regularization parameter α which tapers the exponential function at the crossover wavenumber, therefore retaining the maximum amount of signal with a minimum amount of noise.

Least Squares Spectral Model:

The power spectral estimates for this study were made by calculating the periodogram of the data defined by:

$$I_N(k) = (2/N) \ \left| \ \sum_{n=0}^{N-1} \delta g(n) \ \exp(-ikn) \ \right|^2$$

where k = wavenumber (radians/km)

         N = number of observations

35

$\delta g(n)$ = gravity observations (mGals)

n = distance index.

δx = the spatial sample interval

and $x(n)$ = $n \cdot \delta x$, where $n = 0,1,\ldots,N-1$.

The periodogram is normalized by $N/2$ and sampled at a discrete set of wavenumbers, k_j, determined by the sampling rate of the data as follows:

$$\delta k = 2\pi /(N \, \delta x),$$

where δk = wavenumber sampling interval

and k_j = $j \cdot \delta k$ where $j = 0,1,\ldots,N/2$.

In all periodograms calculated, the data are scaled so that the wavenumber at the Nyquist $= \pi$.

The periodogram is a natural but unsatisfactory estimate of the power spectrum due to its fluctuating form (Priestly, 1981). However, in this study the power spectrum is reduced to a few rough parameters, such as crossover wavenumber and low wavenumber intercept, and the periodogram is found to be an adequate spectral estimate.

In order to find the crossover wavenumber, a technique for distinguishing between signal and noise is needed. Since the spectral shape is composed of a sloping line representing the signal or source and a flat line representing noise, a least squares, line spline approximation to the spectrum seemed appropriate.

The signal portion of the spectrum is fitted separately from the noise. The noise is constrained to have zero slope, and both solutions are constrained to merge at the crossover wavenumber. The correct choice for k_c produces the best least squares fit to the spectrum. Optimization for k_c using this least squares fitting is accomplished with a univariate minimization procedure, FMIN (Forsythe et al., 1977).

In practice, it is necessary to weight the least squares fit to the signal. A weighting scheme with the spectral signal weight being inversely proportional to wavenumber and decreasing linearly works well. The weighting factors are determined a priori with the weight at $k = 0$ equal to one and the weight at the Nyquist is equal to zero. Since the amount of noise in different data sets varies, the weighting factors may need to be adjusted accordingly.

Wavenumber Dependence of the α Parameter:

Once a method for determining k_c is found, a method for choosing the regularization filter with rolloff at the crossover wavenumber depends on finding a relationship between the regularizing parameter, α, and k_c. Some preliminary investigation of the behavior of the parameter α shows that for regularization at a given depth, increasing α by factors of 10 decreases the rate of the filter rolloff (over a range of 10 dB) by a factor

37

of two for a given depth (Figure 11). This rough correlation of α and wavenumber is not observed for either relatively small or large values of α. In the case of small α, rolloff is not observed; rather, the spectrum is flat. The range of α which produces flat spectra decreases with increasing depth as shown by plots of filter width as a function of α for different depths (Figure 12). For large α values, rolloff occurs at very low wavenumbers. Therefore, it appears that for a given depth, α is a function of wavenumber, and a relationship to k_c can be established.

Empirical Relationship of α to k_c as a Function of Continuation Depth:

A procedure is developed to produce statistical data which will establish the empirical relationship between α and k_c. A series of synthetic gravity models are generated at several depths and the gravity effects of the models calculated. The model used initially is a line source since the gravity effect is known and easy to calculate. In addition, the spectrum is not distorted by the effects of source width and depth extent (Spector and Grant, 1970).

The gravity effect of the synthetic model is calculated at depths of $z = 0$ (the observation plane) and $z = d_c$, where d_c is the continuation depth, taken to be 0.9 times source depth. Gaussian random noise is then

38

Figure 11. Plot of $\log_{10}$ of amplitude of the regularization filter as a function of wavenumber. Each plot from 0 to 9 represents a different α value. α values are incremented by a factor of 10.

PLOT OF FILTER AMPLITUDES
FOR DIFFERENT ALPHA VALUES

SAMPLE DEPTH = 0 5 KM
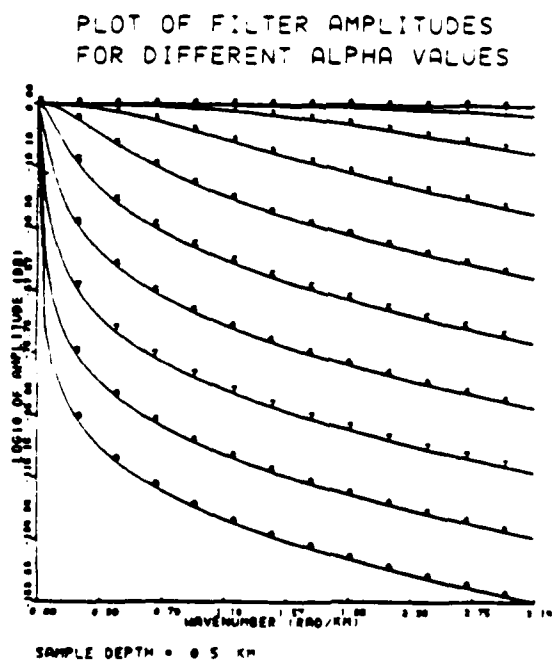
PLOT NO	ALPHA
0	10 0E-4
1	10 0E-3
2	10 0E-2
3	10.0E-1
4	10 0E0
5	10 0E1
6	10 0E2
7	10 0E3
8	10 0E4
9	10 0E5

39

Figure 12. Plot of regularization filter width as a function of the $\log_{10}$ of α for four different depths represented by plots (a) through (d). Filter width is defined as the wavenumber at which amplitude of the filter decays by $1/e$.
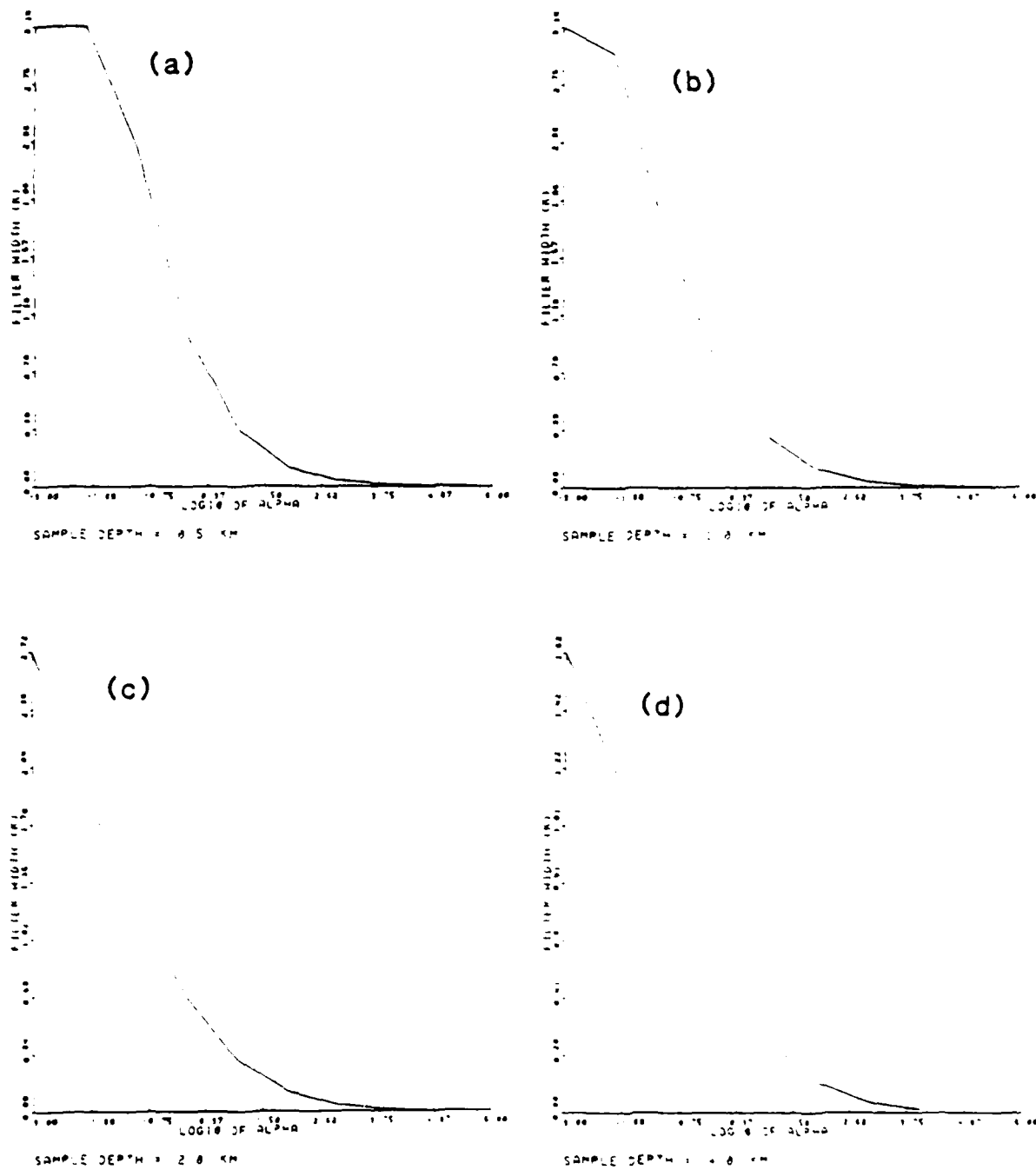
added to the surface data, i.e., superimposed on the data are an additional percentage of normally distributed random numbers. The maximum gravity anomaly value, here defined as the signal level, is used to scale the noise. Note that noise/signal ratio in this case is defined as the ratio of standard deviation of the Gaussian random numbers to the maximum anomaly value and is applicable in in the spatial domain. A distinction is therefore made between spatial noise/signal ratio and noise/signal ratio defining crossover wavenumber in the wavenumber domain. The procedure FMIN is again used to optimize the choice for α by minimizing the least squares error between the surface data after regularization and downward continuation and the actual gravity values calculated at the continuation depth. The crossover wavenumber is chosen by the spectral modeling procedure described previously.

Depths of synthetic models range from 1.25 km to 18 km; depth of the source is doubled after each set of calculations. At each depth, four different noise levels are applied to the data; noise/signal ratios are 0.02, 0.05, 0.10, and 0.20. Figure 13 is an algorithm outlining the experimental procedure. Figure 14 illustrates the results of execution of this procedure for a line source at 6 km (Figure 15) and a noise/signal ratio of 5 percent. Note that the anomaly calculated at

41

Begin

    For j = 1 to n do

        For each j, the depth of the source is doubled; the range of depths is from 0.125 to 18 km

        Generate synthetic gravity data at the surface and at the continuation depth (0.9 times the model depth) for a line source at depth = z_j.

        For i = 1 to 4 do

            noise/signal (n/s) ratio:
            if i = 1 then n/s = 2 percent
            if i = 2 then n/s = 5 percent
            if i = 3 then n/s = 10 percent
            if i = 4 then n/s = 20 percent

            noise to signal ratio = ratio of the standard deviation of the Gaussian random noise to the maximum gravity anomaly value

            Add noise to the surface data.

            Calculate power spectral estimate of surface data.

            Optimize for correct α value by minimizing least squares error between regularized surface data and data at the continuation depth using a nonlinear optimization procedure.

            Find k_c by least squares spectral modeling.

            Filter the data using the regularization and downward continuation functions.

            Calculate least   s error between the filtered surface data and data at the continua   pth.

            Plot results.

        End for

    End for

    Perform linear regression analysis on data from all depths

    Plot α as a logarithmic function of k_c

    Plot the slope of the $\log_{10}$ of α as a function of k_c lines as a function of depth and perform linear regression.

    Plot the α_0 intercept of the $\log_{10}$ of α as a function of k_c lines as a function of depth and perform linear regression

    Derive empirical relationship between α and k_c as a function of depth

End

Figure 13. Experimental procedure to find relationship between the regularization parameter α and crossover wavenumber k_c as a function of depth.

Figure 14. An example of results of the experimental procedure described in Figure 13 for a line source at a single depth: (a) surface data with 5 percent noise/signal ratio, (b) regularization filter with optimal α value of 0.182, (c) comparison of regularized downward continued data with data calculated at the continuation depth (0.9 times the source depth) with rms error of 0.0683 mGals, 9d) least squares spectral model with crossover wavenumber at 0.688 radians/km.
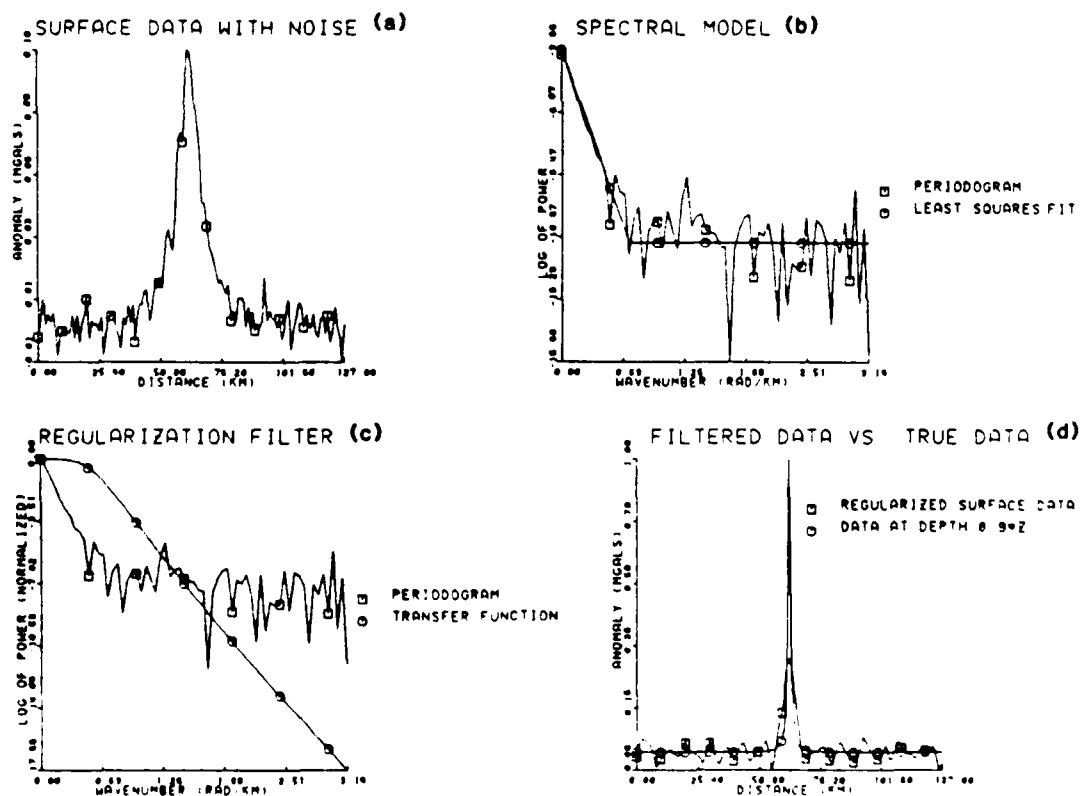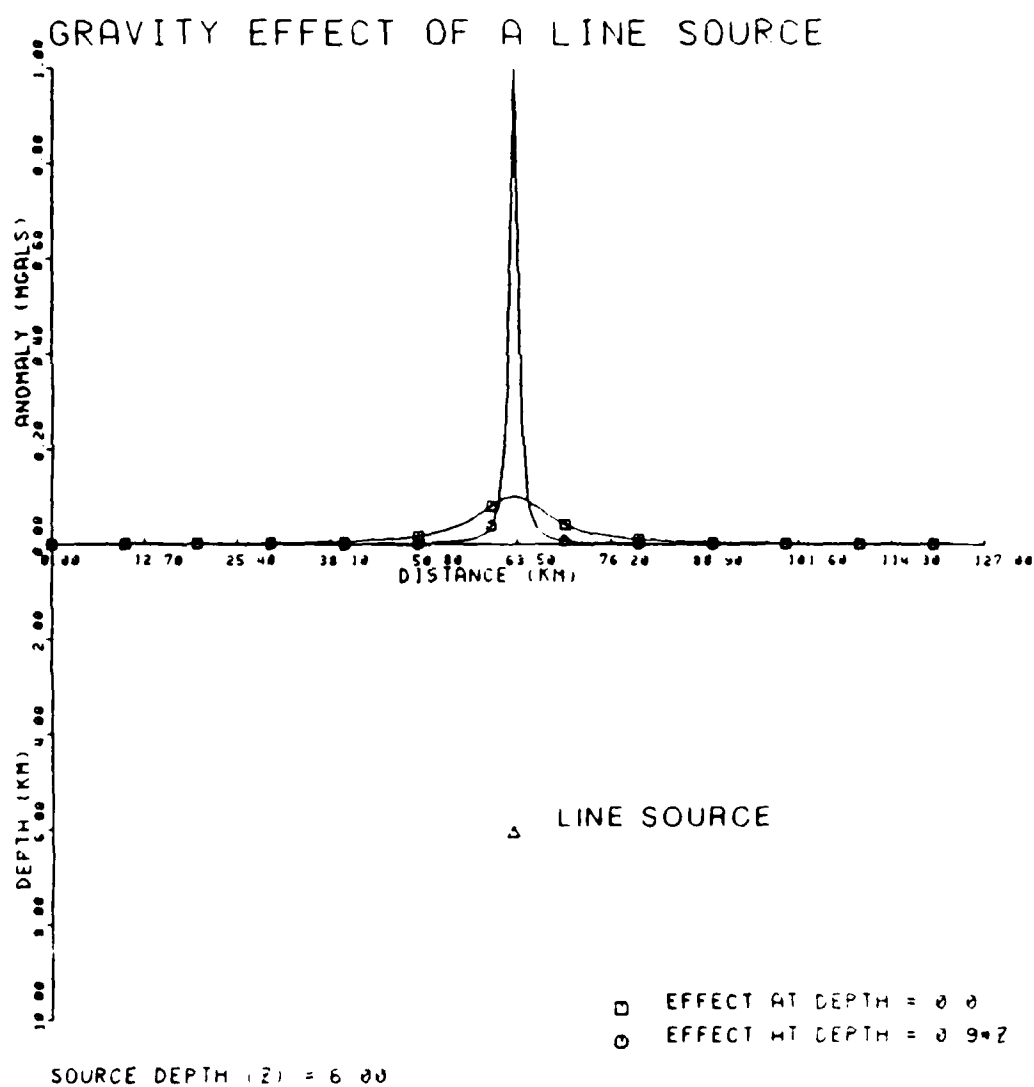
Figure 15. Line source model used to generate synthetic gravity data for the results shown in Figure 14. Depth of the source is 6 km.

GRAVITY EFFECT OF A LINE SOURCE

△ LINE SOURCE

□ EFFECT AT DEPTH = 0 0
○ EFFECT AT DEPTH = 0 9*2

SOURCE DEPTH (Z) = 6 00

the continuation depth closely approximates a delta function, which is expected for a line source. Even though 128 samples were used to define the anomaly, less than 5 percent of the total number of samples defined the peak amplitude. Therefore, even though the filtered signal fits the "true" signal at the continuation depth in a least squares sense, there is a large maximum error between peak amplitudes as the filter can not adequately approximate the sharpness of the true peak amplitude.

The random number generator is reset a total of four times, producing four samples at each noise level for each depth. After the statistical data are obtained, a linear regression analysis of the four data sets is made, and the results are shown in Figure 16, a semi-logarithmic plot of α as a function of crossover wavenumber. As is shown, the log of α can be represented as a linear function of k_c for a given depth. The slope and α-intercept value for the $\log_{10}$ of α (α_0) of each line on Figure 16 are calculated and plotted as a function of depth (Figures 17 and 18). The slopes as a function of depth are linear as are log of α_0 as a function of log of depth. A linear regression analysis of these two factors, slope vs. depth and log of α_0 vs. log of depth, is performed. The coefficients of the linear regression are then used as the empirical relationship for α and k_c, given as:

Figure 16. Plot of $\log_{10}$ of α as a function of k_c for the experimental procedure described in Figure 13. Each line represents a least squares fit to data for a different depth. Depths range from 0.125 to 18 km. The equation in the figure expresses the relationship of α to k_c as a function of depth based on these results.

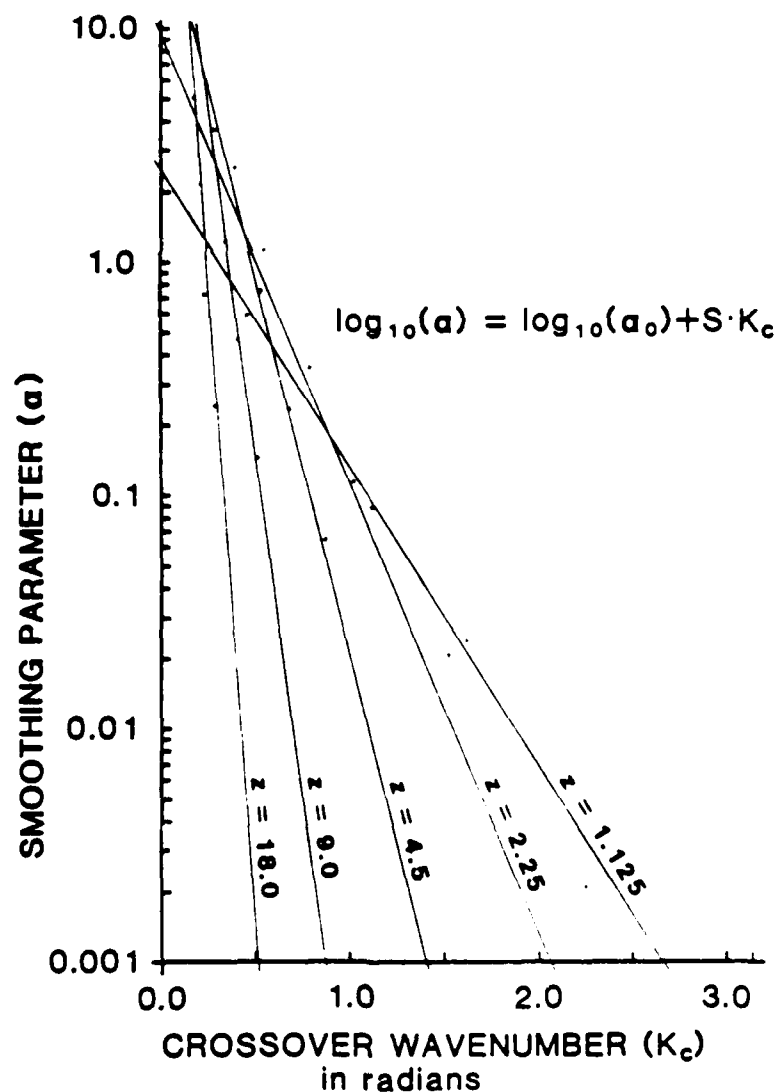
$$\log_{10}(a) = \log_{10}(a_0) + S \cdot K_c$$

Figure 17. Least squares fit of slope of the α vs. k_c lines as a function of depth. The equation expressing the least squares fit is shown.
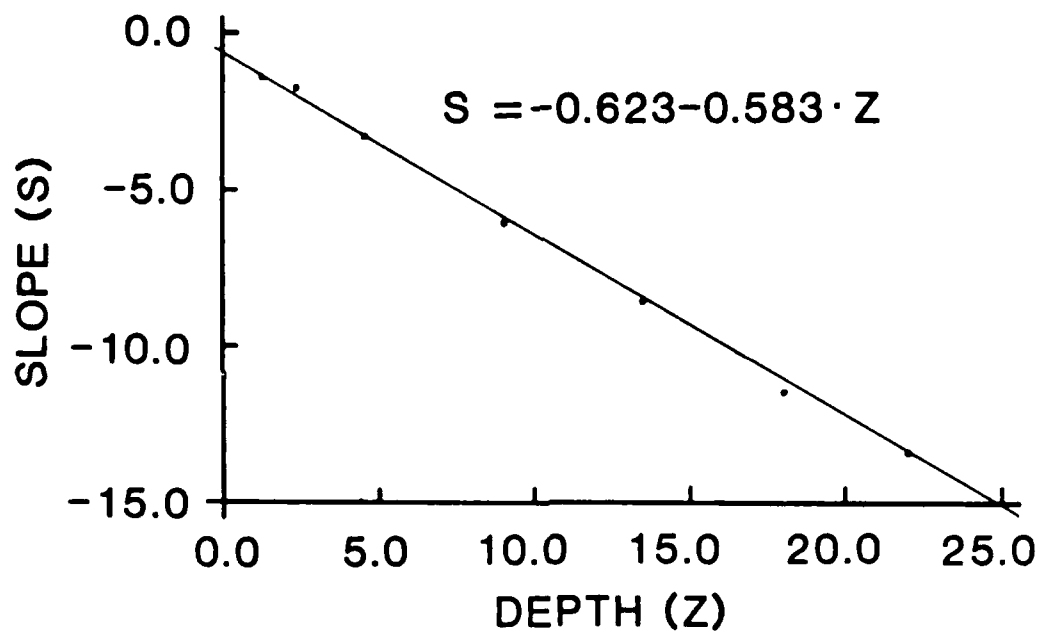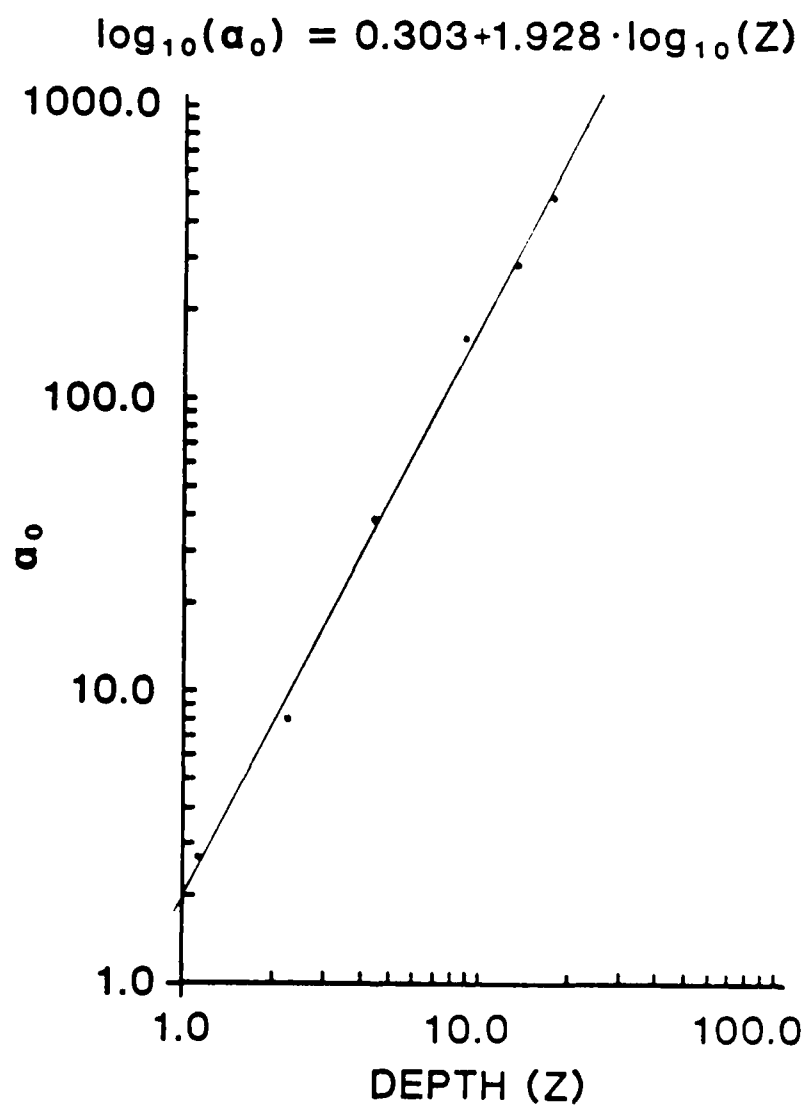

$$S = -0.623 - 0.583 \cdot Z$$

Figure 18. Least squares fit of α_0 intercept of the α vs. k_c lines as a function of depth. The equation expressing the least squares fit is also shown.

$$\log_{10}(\alpha_0) = 0.303 + 1.928 \cdot \log_{10}(Z)$$

$$\log_{10}(\alpha) = \log_{10}(\alpha_0) + S \cdot k_c \qquad \text{(a)}$$

$$S = -0.623 - 0.583 \cdot z \qquad \text{(b)}$$

$$\log_{10}(\alpha_0) = 0.303 + 1.928 \cdot \log_{10}(z) \qquad \text{(c)}$$

From relationships (a), (b), and (c), an optimal value for α could be calculated for any given depth and crossover wavenumber.

Since only a small range of depths are used to establish this relationship, some error might be expected for larger or smaller depths. At the smaller depths (0.0625 km and less), the linear relationship does not strictly hold, but this may be due to a lack of computer precision with α values on the order of 10 and less. Depths greater than about 20.0 km cannot be calculated due to machine overflows from attempted calculation of the exponential, downward continuation function at greater depths.

In spite of a lack of greater depth range, it appears that α is not a highly sensitive parameter. For example, at 1.250 km, standard deviation of α values for a given noise level could range from 10 percent of the average α value at a low noise level to 50 percent of the average α value at a higher noise level. Despite this high variance, rms error between surface data regularized with optimal α and data at depth d_c ranges from between 4 percent and 6 percent of the maximum value of the true

49

gravity anomaly at depth, the error level increasing with increasing noise level.

Regularization with Optimal Selection of α:

The empirical relationship between α and k_c described in the last section is tested on a synthetic gravity model distinct from the model used to generate the experimental data. The gravity effect of rectangular prismatic sources at different depths is calculated at the observation plane, $z = 0$, and at the continuation depth, d_c, and the procedure of Figure 19, as described below, is followed to test the accuracy of the empirical α-k_c relationship. For each depth, width of the source ranges from 0.1 to 1.6 times the depth of the source. Depth extent of the source is one fourth of the source depth for each test case. Source width is varied in order to monitor the effect of finite source thickness on efficiency of the regularization filter. The α parameter produced by the empirical relationship formula compares favorably with the "optimal" α value calculated using the procedure FMIN as previously described. Variations on the order of 10 to 20 percent are observed between the α values using the two different methods.

Rms error between regularized, downward continued data and data calculated at the continuation depth ranges from 5 to 8 percent. Again, the greatest error is observed between filtered and "true" data at higher noise

Begin

For j = 1 to n do

For each j, the depth of the source is doubled; the range of depths is from 0.125 to 18 km

For k = 1 to m do

For each k, the width of the source is doubled; the range of widths is from 0.1 to 1.6 times the depth of the source. The depth extent of the source is constant at 0.25 times the depth of the source

Generate synthetic gravity data at the surface and at the continuation depth (0.9 times the model depth) for a rectangular source at depth = z_j.

For i = 1 to 4 do

noise/signal ratio (n/s):
if i = 1 then n/s = 2 percent
if i = 2 then n/s = 5 percent
if i = 3 then n/s = 10 percent
if i = 4 then n/s = 20 percent

noise to signal ratio = ratio of the standard deviation of the Gaussian random noise to the maximum gravity anomaly value

Add noise to the surface data.

Calculate power spectral estimate of surface data

Find k_c by least squares spectral modeling.

Find α using empirical $\alpha - k_c$ relationship for the continuation depth $0.9*z_j$.

Filter the data using the regularization and downward continuation functions.

Calculate least squares error between the filtered surface data and data at the continuation depth.

Compare these results with results obtained using the α value obtained from the nonlinear optimization procedure.

Plot results.

End for

End for

End for

End

Figure 19. Procedure for testing rectangular source models using previously derived, empirical α vs. k_c relationship as a function of depth.

51

levels. Increasing the width of the source does not increase the error; however, error level for the rectangular sources is higher than that observed for line source anomalies. A representative example of one of the sources used (Figure 20) and results for two different noise/signal ratios (0.05 and 0.20) (Figures 21 and 22) are presented.

Testing the Forward Solution:

The one-dimensional Fourier forward gravity solution with the addition of a vertically varying density function is tested on a synthetic trapezoidal model (Figure 23); the density function is arbitrarily chosen and specified a priori. Results of the forward solution are compared to results obtained from a constant density, forward gravity technique which sums the gravity effects of prismatic bodies (Corbato, 1965). A linear density function is simulated for the constant density solution by calculating the gravity effect of multiple layers. Density contrast at each layer is equal to the value of the specified density function at the midpoint of each layer. This corresponds to a straight numerical solution of the field integral. Increasing the number of layers alters the results only slightly and does not lessen variation of the gravity anomaly values between the two methods; therefore, resolution of the field integral method is not increased as a result of

52

Figure 20. Example of rectangular source model at 6 km

depth and gravity effects calculated at the surface or

observation plane (z = 0) and at the continuation depth
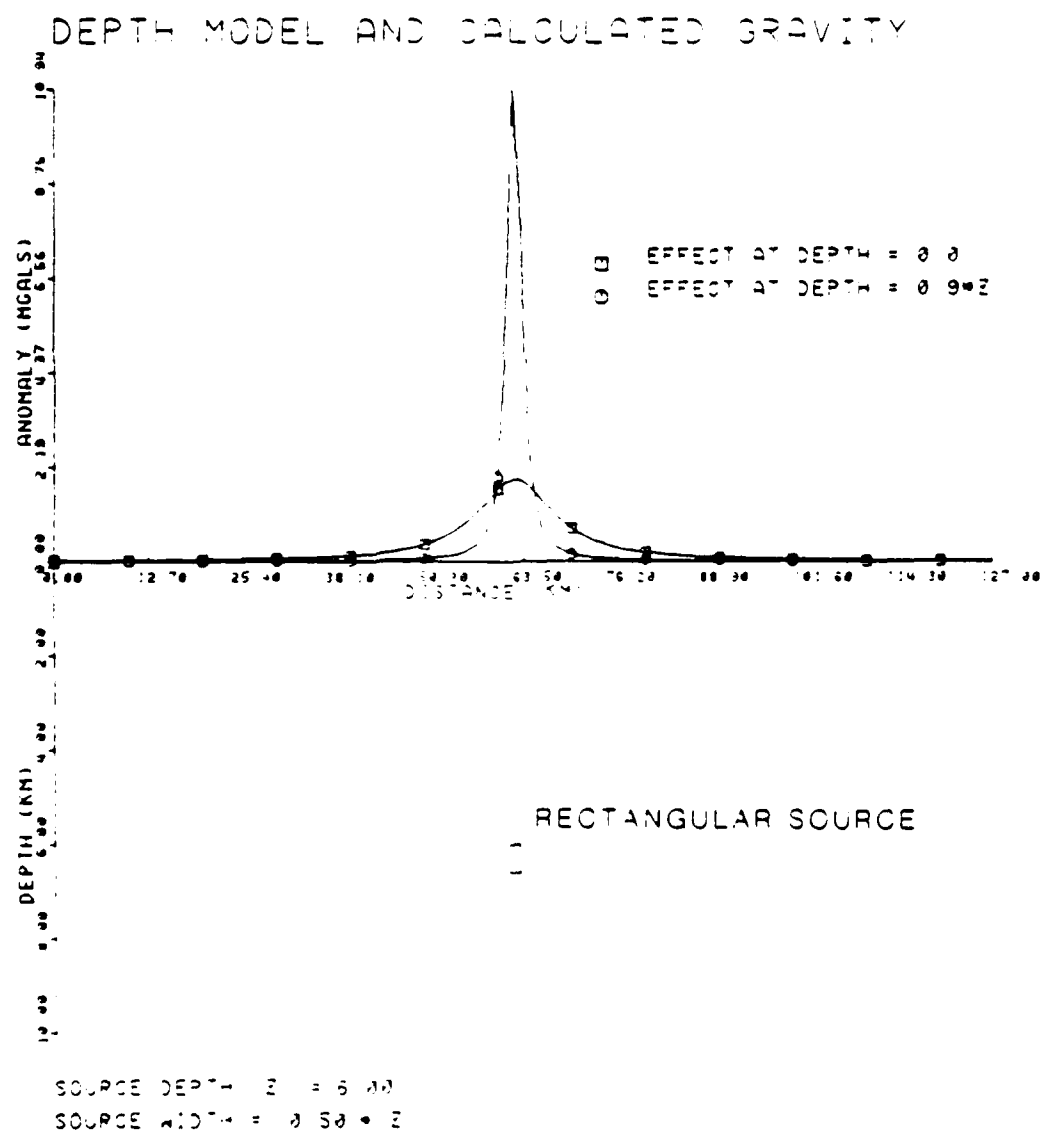
(z = d_c) where d_c = 0.9 times the source depth.

Figure 21. Example of results of applying the procedure described in Figure 19 for the source in Figure 20 using empirical α vs. k_c relationship as a function of depth: (a) surface data with 2 percent noise/signal ratio, (b) spectral model with k_c at 0.679 radians/km, (c) regularization filter plotted with the data spectrum and $\alpha = 0.143$, (d) comparison of regularized, downward continued surface data with data calculated at the continuation depth (5.4 km) with an rms error of 0.8016 mGals.
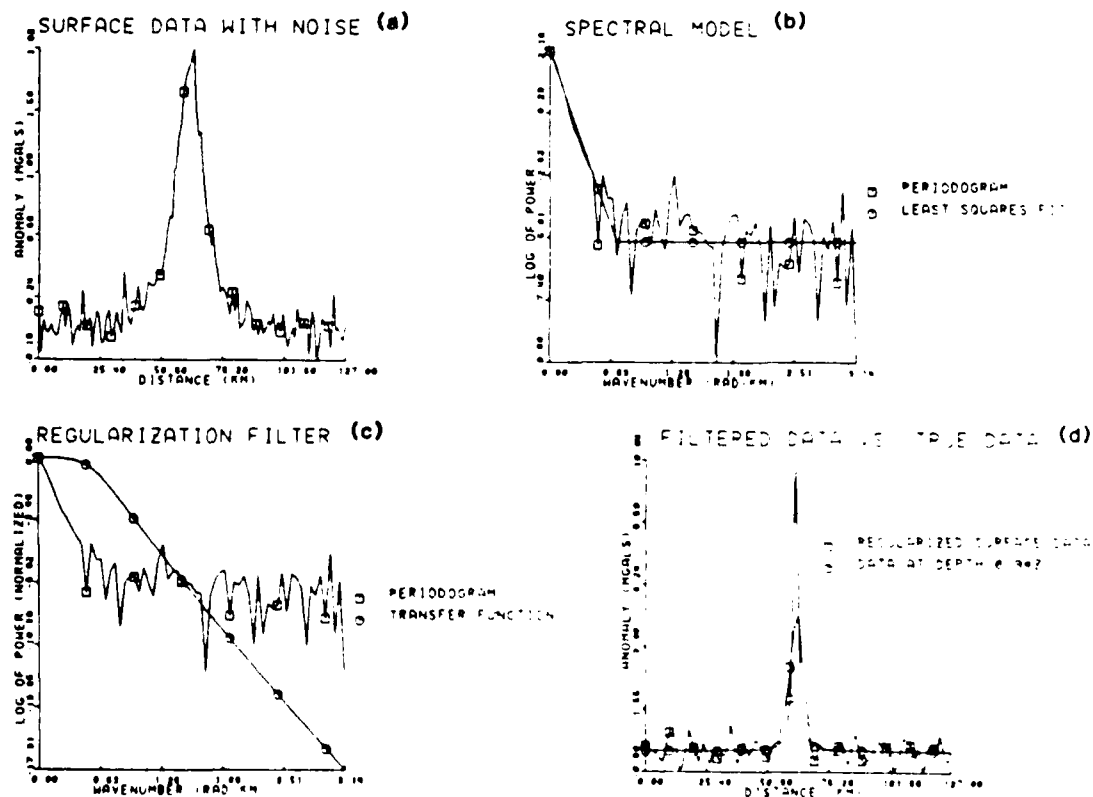
Figure 22. Results using the same model as in Figure 21 with noise/signal ratio of 20 percent: (a) surface data with added noise, (b) spectral model with k_c at 0.405 radians/km, (c) regularization filter plotted with data spectrum and $\alpha = 1.547$, (d) comparison of regularized, downward continued surface data with data calculated at the continuation depth (5.4 km) with an rms error of 0.8965 mGals.
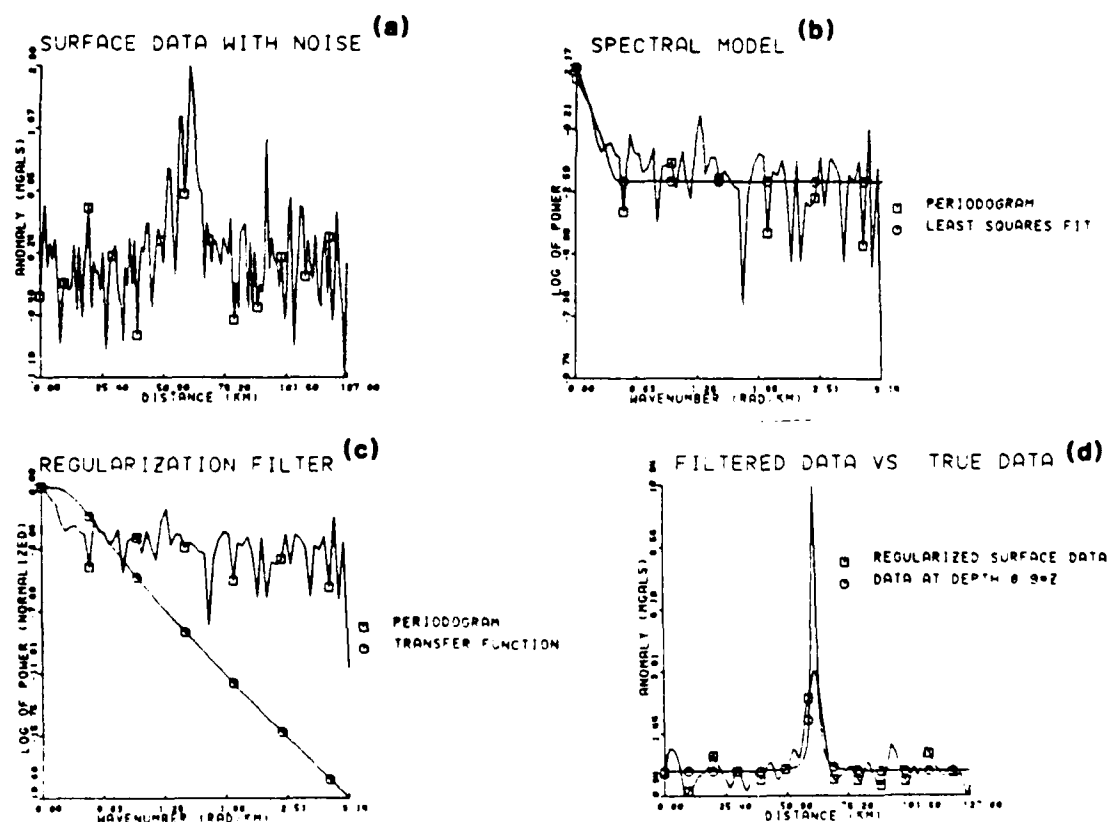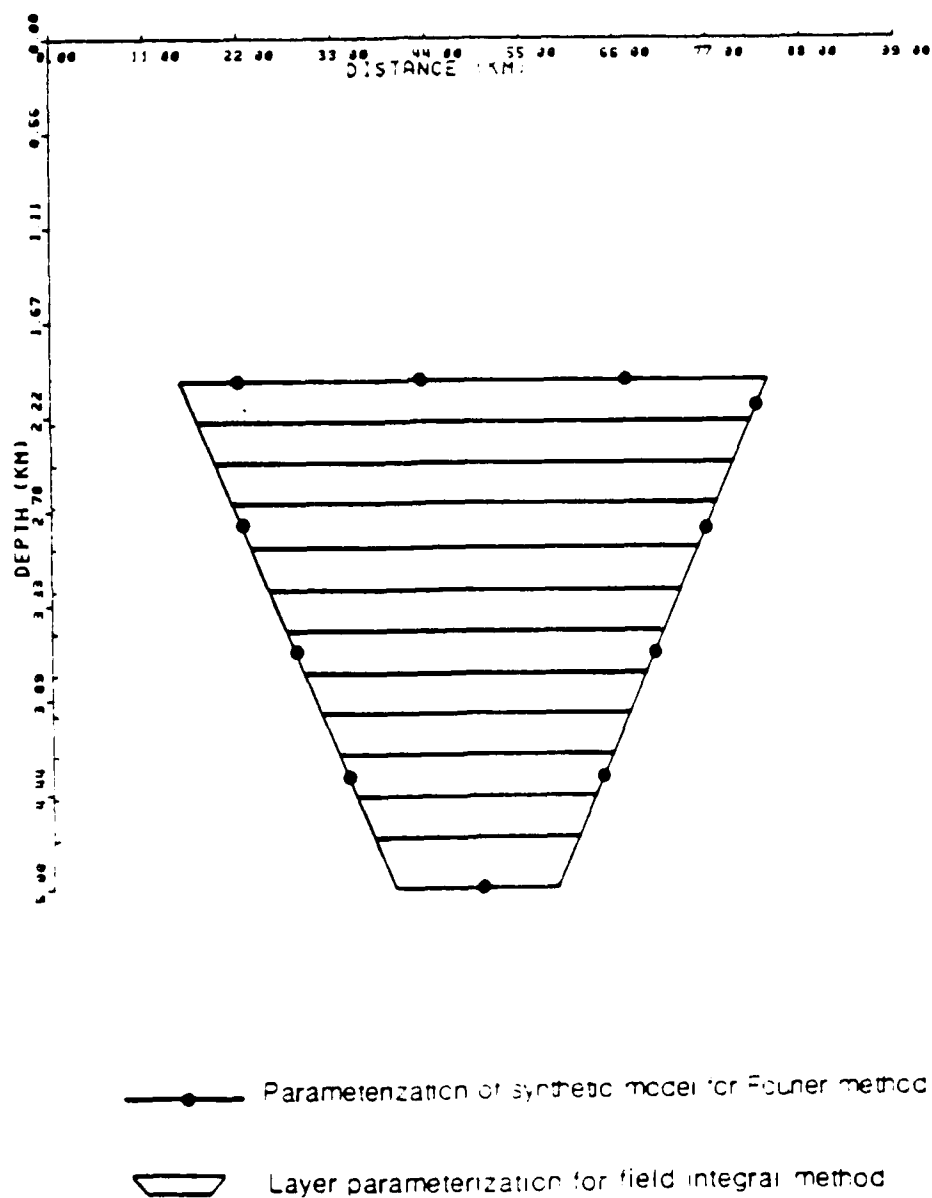
Figure 23. Synthetic trapezoidal model used to test the Fourier forward gravity algorithm with linear density function.

increasing the parameterization. Results presented here are calculated with a 12 layer model. The Fourier solution is compared with summed results of the field integral solution. Rms error between the two results is 1.43 mGals (4.1 percent error) and maximum error is 3.25 mGals (9.4 percent error) with greatest error occurring along the flanks of the anomaly (Figure 24). Discrepancy between the two methods can be attributed to a difference in source parameterization. For the field integral method, each layer is parameterized with four vertices and a single density contrast. Model parameterization for the Fourier calculation assumes a continuous body sampled at discrete intervals with a smoothly varying, linear density function. The difference is most pronounced in its affect at the shallow body corners.

Testing the Inverse Solution:

The inverse solution is tested using a synthetic, basin-type gravity model. Gaussian random noise is added to gravity anomaly values calculated from the synthetic model. In addition, data are pre-processed by applying a 5 percent cosine taper and padding the data with zeros out to twice the interval length. An initial guess for the model is made using a Bouguer slab approximation,

$$d_i = \delta g_i / (2 \pi G c) ,$$

where:

$$d_i = \text{slab thickness}$$

Figure 24.   Results of testing the Fourier forward gravity algorithm against the field integral solution of Corbato (1965) for the model of Figure 23. differences along the sides of the anomaly are probably due to differences in model parameterization
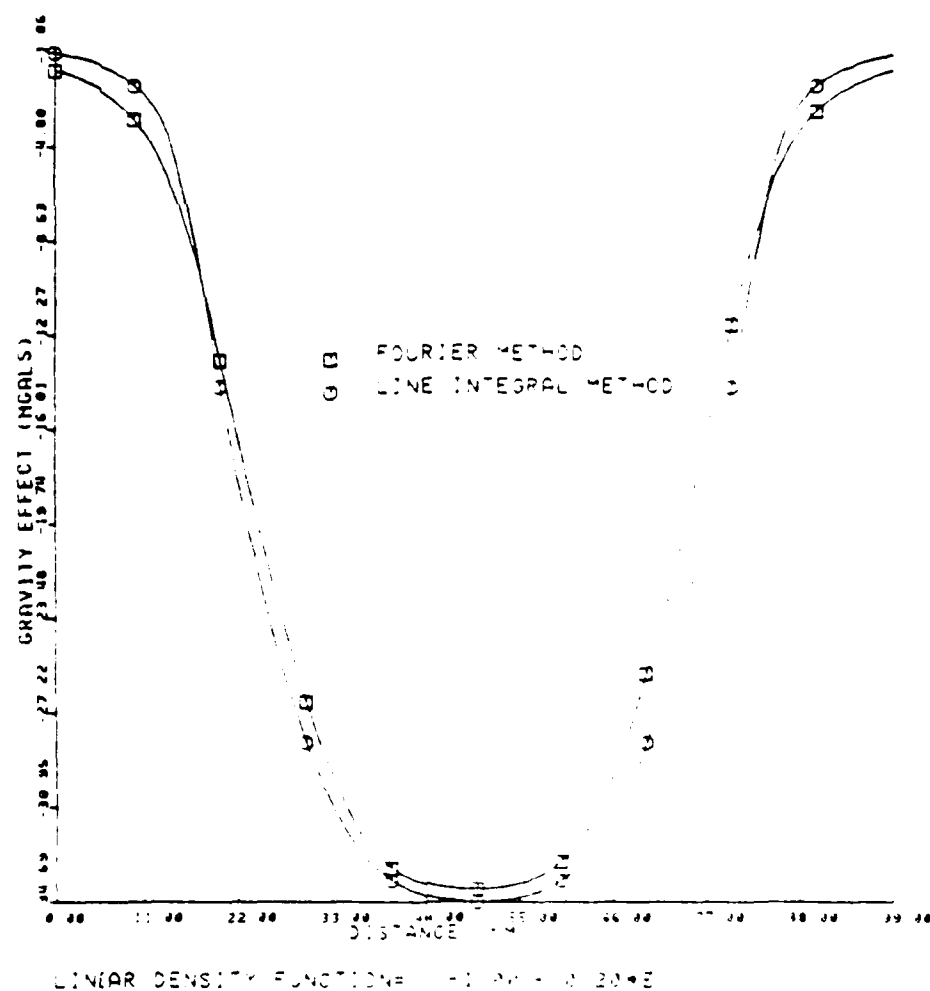
σ = density contrast

δg_i = pre-processed gravity data

and,

i = 1 to N, where N = length of data interval.

A first approximation to the continuation depth used in the choice for α and in the regularization filter is a depth halfway between minimum and maximum model depths estimated by the Bouguer slab formula for the initial guess. Density contrast used in the initial guess is specified a priori and is the value of the specified density function midway between a minimum and maximum model depth estimate.

The inverse modeling procedure as adapted from Ferguson et al. (1988) is shown in Figure 25. The data are regularized using the empirical α-k_c relationship, with crossover wavenumber determined by the spectral modeling procedure previously discussed and continuation depth estimated from the initial guess. After each iteration of the inversion algorithm, a new model is generated and used in the forward algorithm to generate synthetic gravity data. Synthetic data are compared with observational data and rate of change of the ratio of rms error between the two data sets from the previous to present solution is used to determine convergence of the solution. If convergence is not obtained, the continuation depth of the present model is used to

Begin

    Read data and compute initial guess model.

    Take Fourier transform of data.

    Calculate power spectral estimate of data.

    Find crossover frequency (k_c) using least squares spectral modeling.

    Find regularization parameter, α, using empirical α vs. k_c relationship as a function of continuation depth (z_c).

    Perform one evaluation of Fourier forward gravity algorithm using initial guess model and calculate error between theoretical and observed data to set initial rms error level.

    While the number of iterations is less than the maximum (specified a priori) and the ratio of current to previous least squares error is greater or equal to the tolerance level (specified a priori) do

        Take Fourier transform of data.

        Filter the data using the regularization function.

        Invert the data using the Fourier gravity inversion algorithm.

        Find new α using empirical relationship at new z_c.

        Filter the model using the regularization function.

        Calculate theoretical gravity data by using the new model in an iteration of the Fourier forward gravity algorithm.

        Find the least squares error between the observed and theoretical data

        Calculate ratio of current to previous least squares error.

    End while

    Plot the results.

End

Figure 25. Procedure for inversion of gravity data using regularization and the Fourier gravity inversion technique with a linear, vertically varying density function.

regularize the original data and another iteration is then performed.

In practice, rms error is "windowed" so as not to extend beyond the length of the original interval of observations. Windowing the error speeds convergence due to exclusion of error from any Gibbs oscillation along the edges of the anomaly, that error having greater weight than error due to a misfit of data representing deeper portions of the model. Differential error weights result since density is a function of depth. Resolution at greater depths is less as the value of the density contrast is less (for a negative density contrast) resulting in a disparity in the contribution to the overall gravity effect between deep and shallow components. Without windowing, this disparity tends to bias the inversion procedure toward a better fit of the data on the sides of the anomaly rather than on the peak.

Convergence criteria are determined a priori. In general, a maximum of ten iterations are sufficient and rate of change of the ratio of least squares error between synthetic and calculated gravity anomaly values of between one and five percent is considered satisfactory. Speed of convergence depends on a reasonable initial guess of the gravity model; a good initial guess reduces the number of iterations required for convergence. Underestimating the density contrast

61

used in initial depth estimates tends to produce models which underestimate depth of the source and converges more slowly. Overestimation of the density contrast results in more rapid convergence; however, if model depths obtained from initial guess estimates occur at depths which exceed the saturation level of the density function, the solution diverges.

For synthetic model results, an rms error of 2.52 mGals or about 3 percent of the maximum gravity anomaly value is observed; however, effects of the addition of noise with a 2 percent noise/signal ratio are completely filtered out (Figure 26). Rms error between the gravity model obtained from inversion and the synthetic model (Figure 27) is 0.087 km or about 2 percent of the maximum depth whereas maximum error is 0.18 km or about 4.5 percent error.

For comparison, the same synthetic model is used and a noise/signal ratio 5 percent is added to the synthetic gravity data. The final anomaly fits the synthetic anomaly very well in a least squares sense, with an rms error of 4.3 mGals or 5 percent of the maximum anomaly value (Figure 28). Model depths also compare favorably at the higher noise level (Figure 29) with an rms error of 0.11 km or 2.7 percent and maximum error of 0.25 km or 6.3 percent. Greatest error in both cases occurs along the sides of the model, but error in

Figure 26. Comparison of theoretical data calculated from gravity model obtained from the inversion procedure of Figure 25 compared with gravity data calculated froma synthetic basin type model with 2 percent noise/signal ratio.

63

Figure 27. Synthetic basin type model used to generate
gravity data shown in Figure 26 compared with final
gravity model calculated from inversion procedure of
Figure 25. The density function used in the modeling
is indicated in the figure.

Figure 28. Comparison of theoretical data calculated from gravity model obtained from the inversion procedure of Figure 25 compared with gravity data calculated from a synthetic basin type model with 5 percent noise/signal ratio.
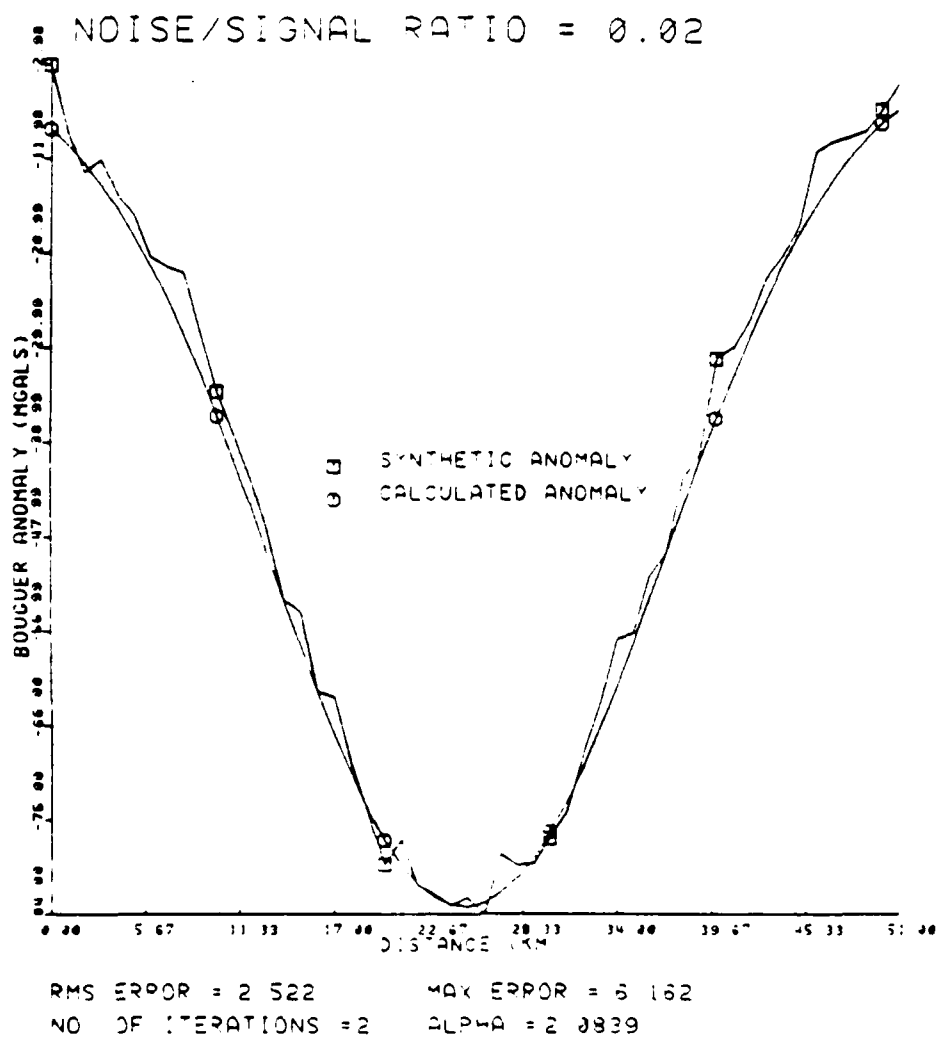
Figure 29. Synthetic basin type model used to generate gravity data shown in Figure 28 compared with final gravity model calculated from inversion procedure of F ⁻e 25. the density function used in the modeling is indicated in the figure.
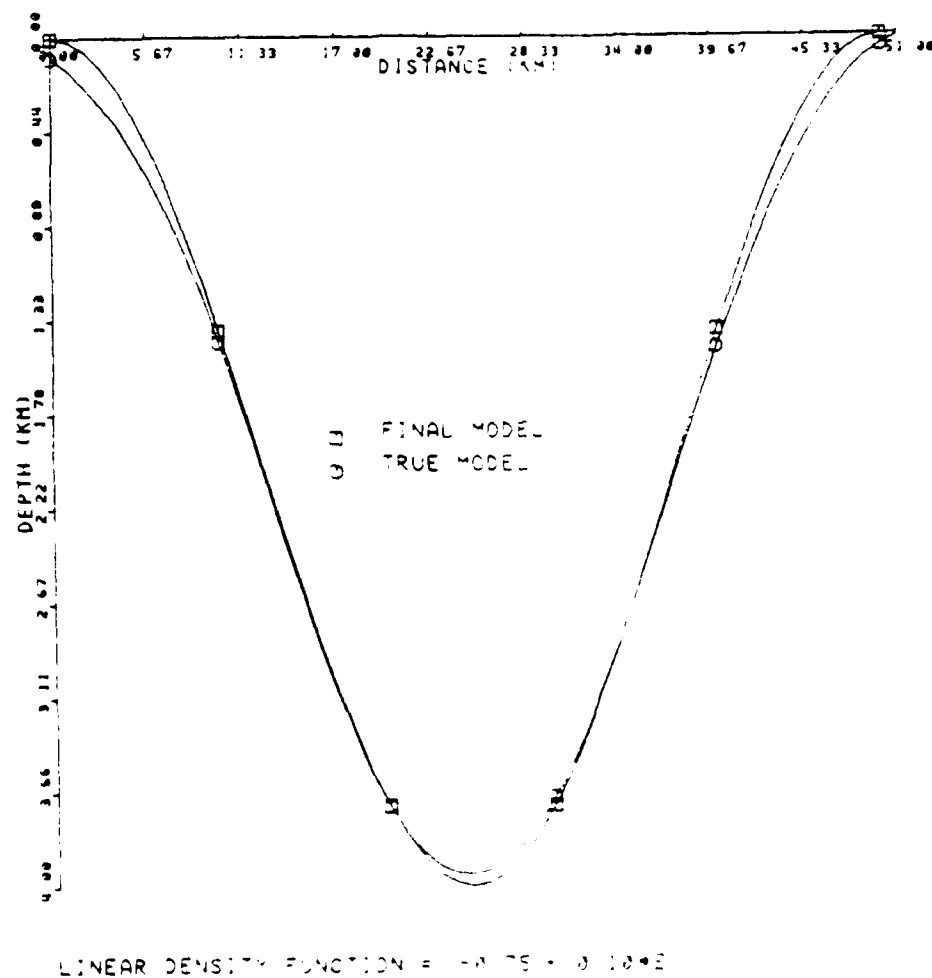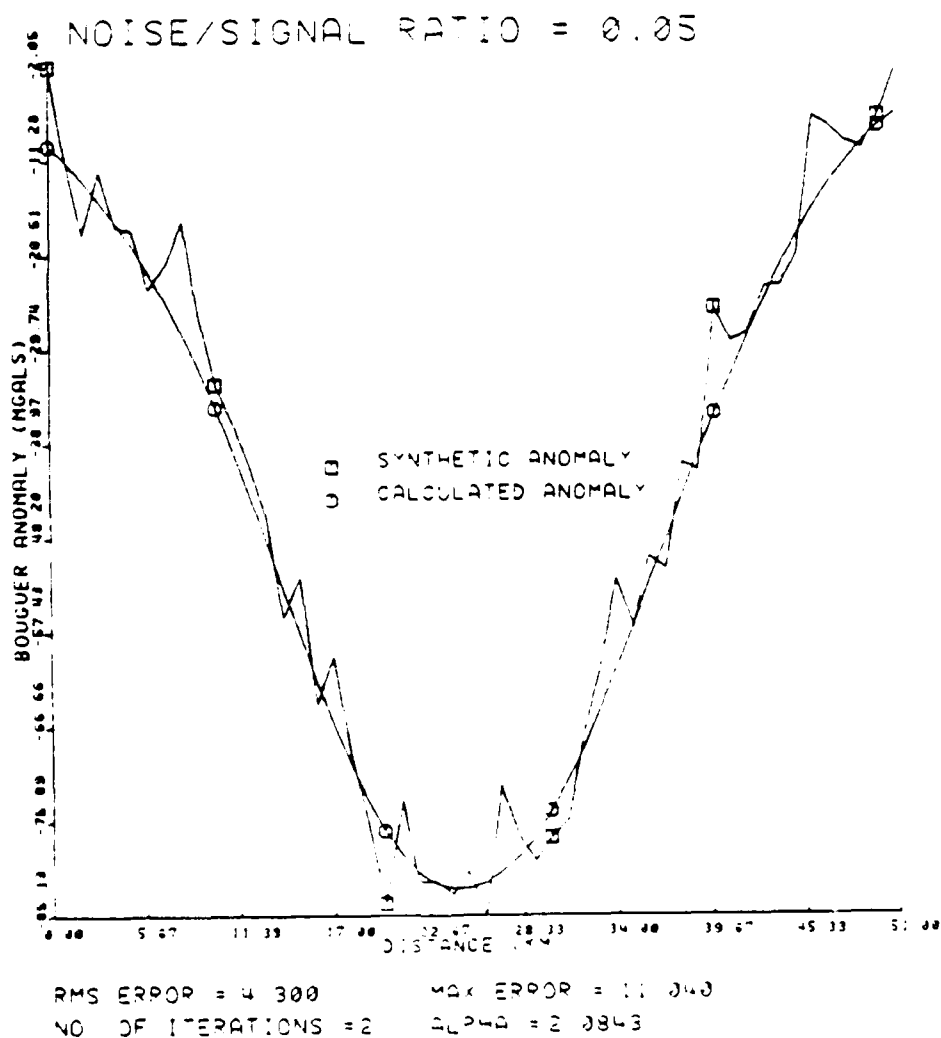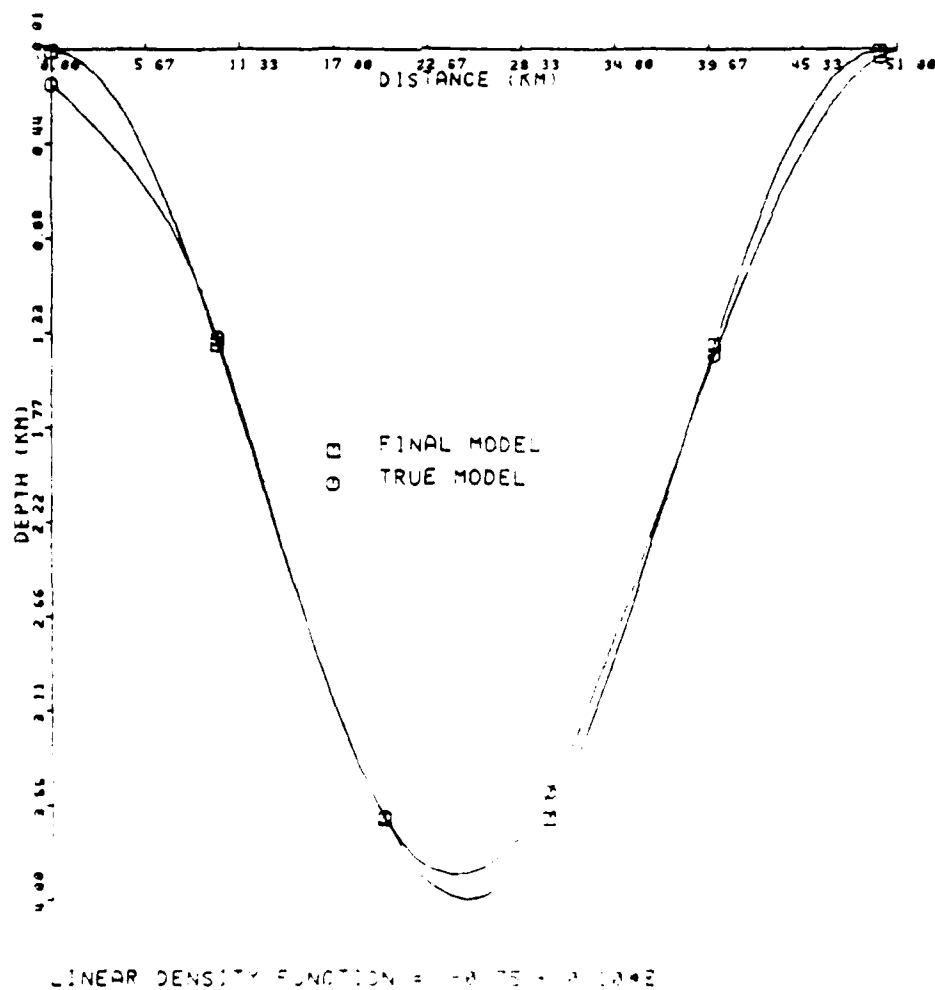

LINEAR DENSITY FUNCTION = -.78 75 + .9 .0048

both cases is considered well within acceptable error bounds.

Error level can be decomposed into contributions from observational error, the added noise level, and resolving error, resulting from suppression of high wavenumber information during regularization. Since the regularization filter is optimized based on the assumption of sources at depth, resolution of the model along the shallow flanks of is poorer as the corresponding short wavelength information is filtered out. Width of the regularization filter is a qualitative measure of model resolution (Ferguson et al., 1988). Since for both noise levels crossover wavenumber is relatively small (Figure 30), bandwidth of the low pass, regularization filter is also small resulting in a lack of resolution as observed along the edges of the synthetic basin-type model.

Figure 30. Spectral models for the data generated by the synthetic basin type model with: (a) 2 percent and (b) 5 percent noise/signal ratios. Note the slight shift toward low wavenumber for crossover wavenumber of the higher noise/signal ratio.

Spectral Models
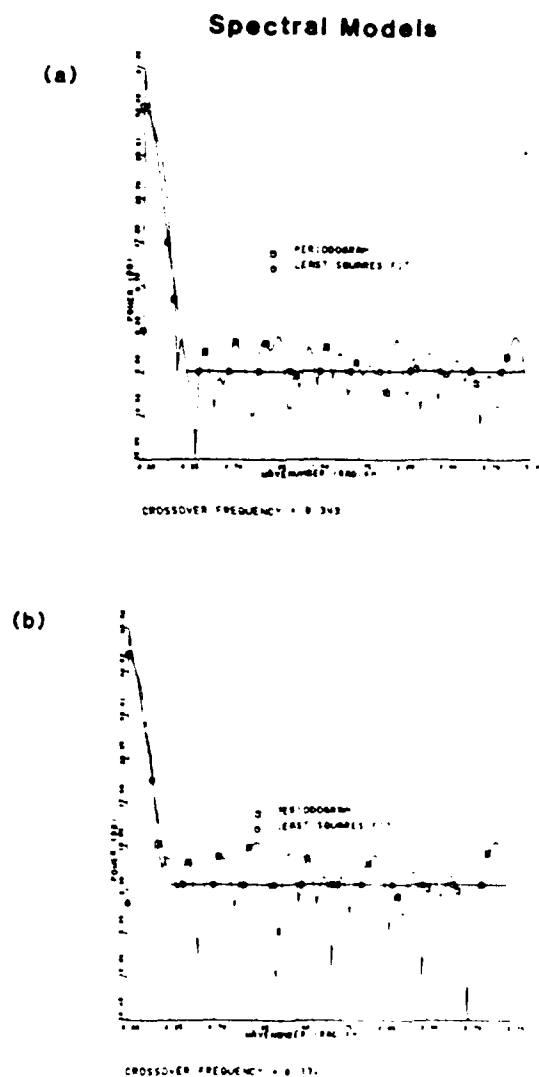
Collection and Reduction of Gravity Data
at Pahute Mesa, Nevada

The data used in this study consist of approximately 1700 gravity stations collected by the USGS and the University of Texas at Dallas (UTD). Approximately 250 gravity stations and elevations were collected by UTD in June, 1985 at Pahute Mesa, Nevada along detailed survey lines (station spacing of approximately 0.3 km). The gravity data were collected with two LaCoste and Romberg gravimeters and elevations were shot in at each station with a Zeiss Elta-4 electronic distance meter. The accuracy of these stations is probably good to within ±0.5 mGals. The detailed gravity stations were merged with the existing approximately 1400 USGS gravity stations at Pahute Mesa (Figure 31). The accuracy of the existing data is approximately ±5 mGals (Healy, 1968). After merging the two data sets, the data were edited and stations deleted that were considered bad points.

The complete Bouguer anomaly map of Pahute Mesa (Figure 32) was obtained by the following reduction procedure. Hand terrain corrections of Hammer zones B-D (Hammer, 1939) were calculated for both data sets and added to outer zone terrain corrections calculated from the terrain correction program of Plouff (1977). Total terrain corrections ranged from about 0.2 to 2.0 mGals.

69

Figure 31. Location plot of 1728 gravity stations in Pahute Mesa, Nevada from merged USGS and UTD data. The outline of Silent Canyon caldera and model profiles A-A' and B-B' are indicated.
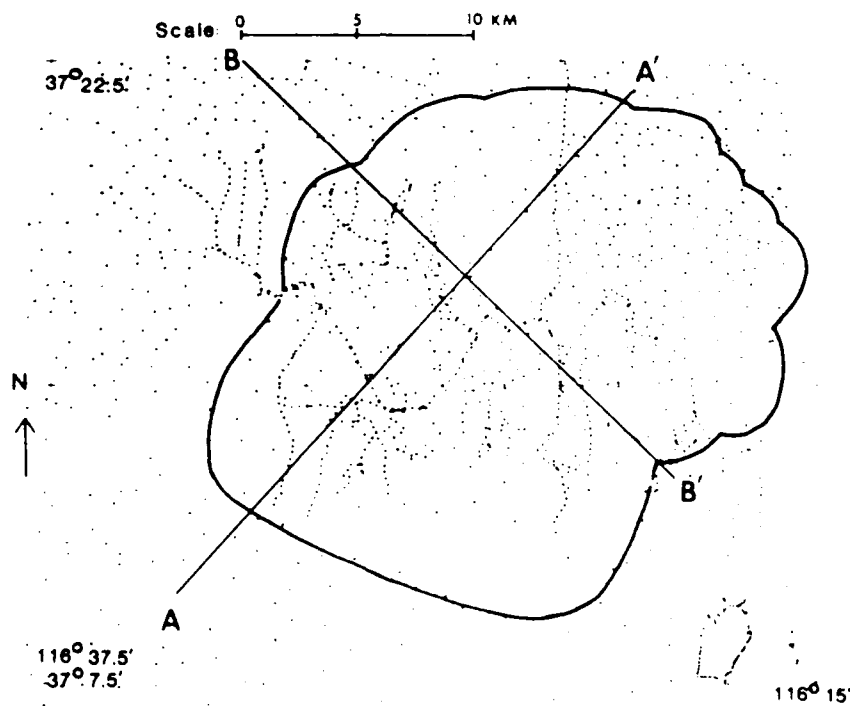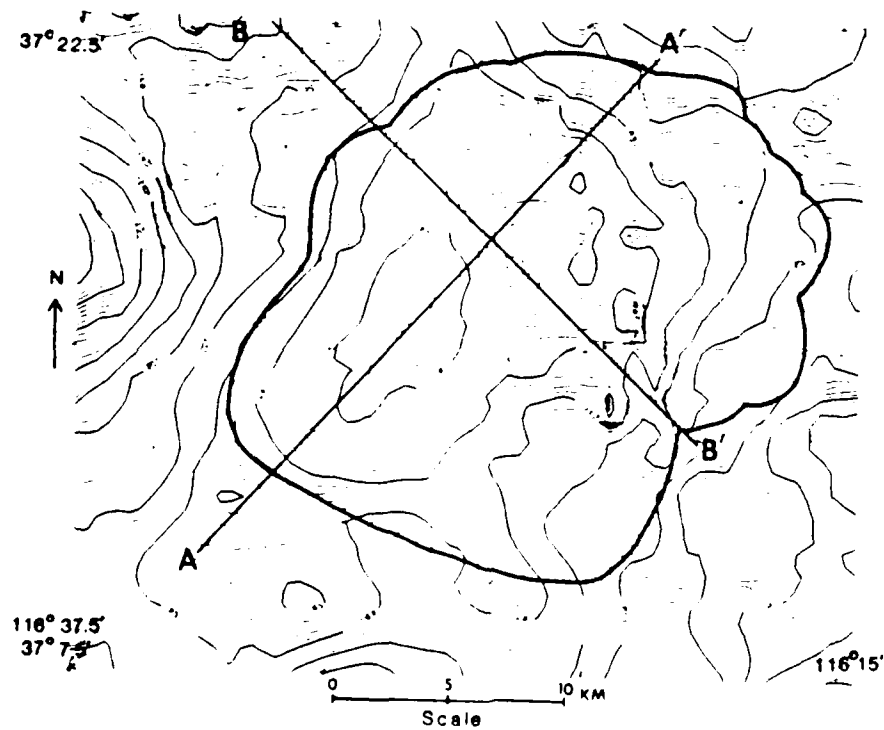
Figure 32. Complete Bouguer anomaly map of Pahute
Mesa, Nevada using USGS data merged with UTD data.
Contour interval = 1 mGal. Reduction density = 2000
kg/m^3. The outline of silent Canyon caldera and model
profiles A-A' and B-B' are indicated.

Reduction density for the complete Bouguer anomaly was 2000 kg/m . This density was an average density of the rocks constituting the topography at Pahute Mesa down to a depth of about 0.15 km, which ranged from about 1600 to 2200 kg/m , estimated from analysis of average densities obtained from borehole gravity logs. The data were gridded at 0.5 km intervals and contoured at 1 mGal.

Possible error in the UTD data could be attributed to a number of factors. A list of some of these factors is given below.

1. Equipment failure. Equipment failed on several occasions due to afternoon high temperatures at Pahute Mesa, sometimes well over 100 F. Parts of the survey where this occurred were redone; however, the possibility of error remains.

2. Observational error. Repeatability to within 0.01 mGals was required for each gravity station, to within ±1.5 meters for vertical distances, and to within ±0.030 kilometers for horizontal distances. Some error is to be expected from inaccurate posting of the data or inaccurate reading of instruments.

3. Plotting error. When converting digital survey data to map data, some plotting errors can be expected. In this case, the data was plotted by hand onto a base map at a scale of 1:24000, and the x-y locations for each station were digitized from the base map. Horizontal

locations at this scale are only good to about ± 0.030 kilometers.

A Pahute Mesa Gravity Model

The inversion procedure is tested next on observational gravity data from Pahute Mesa, Nevada. A complete Bouguer anomaly map of the area, contoured at one mGal and with a reduction density of 2000 kg/m^3, is shown in Figure 32 with model profiles A-A' and B-B' indicated. Station locations are shown in Figure 31. Only profile B-B' will be discussed in this report, due to unresolved stratigraphic details along A-A'.

Profile locations are chosen parallel (A-A') and perpendicular (B-B') to the northeast-trending, elliptically-shaped gravity low over Pahute Mesa thought to outline Silent Canyon caldera (Healy, 1968; Orkild et al., 1968). The caldera rim, as outlined by steepening of the gravity contours, is obscured to the southwest due to thickening of Timber Mountain volcanics (Orkild et al., 1968). Based on the density structure of Pahute Mesa, Silent Canyon caldera can be modeled as a higher-density half space corresponding to the Belted Range Tuff below a lower density layer, the caldera fill. Therefore, this is essentially a basin-type model. Based on this assumption, choice of the Fourier gravity inversion technique seems appropriate as the model parameters produced by the inversion will delineate a detailed model of the caldera at the interface between

74

the Belted Range tuff and the caldera fill. The addition of a vertically varying, linear density function makes it possible to fit the linear density vs. depth relationship as discussed earlier into the model.

In order to constrain the regional anomaly, profiles have been extended outside the edges of the caldera to gravity stations resting on outcrops of rocks representing the gravity basement, i.e., the Belted Range tuff or an equivalent lithology. Profile B-B' is constructed to extend northwest from outcrop of the Grouse Canyon member of the Belted Range Tuff southeast to outcrop of Quartet Dome lavas. Quartet Dome lavas are lithologically equivalent to (i.e., have about the same density contrast as) and are found interbedded with Grouse Canyon tuffs.

The observed anomaly is assumed to be the sum of two components, (1) a regional anomaly of wavelength equal to or greater than the profile length and (2) a residual anomaly composed of smaller wavelength effects (Nettleton, 1976). Based on the assumption that the Pahute Mesa gravity low is caused by lower density caldera fill, the residual gravity anomaly at basement outcrops at either end of the profiles should be zero. Therefore, the regional anomaly at either profile terminus is defined by the observed Bouguer anomaly value at that location. Shape of the regional anomaly is

assumed to be a low order surface with wavelength proportional to the profile length. The regional anomaly for Pahute Mesa is fitted with a second degree polynomial.

The regional anomaly calculation is incorporated into the modeling procedure using a method adapted from Ferguson et al. (1988) (Figure 33). Boreholes in Pahute Mesa which penetrate the basement along each profile line are used to constrain the regional (Figure 34). As outlined in Figure 33, after each gravity inversion, a new model is produced. Model depths are compared to borehole depths and residual errors used to calculate a new regional anomaly. After removal of the new regional, another new model is calculated. The modeling process is terminated when residual error between borehole depths to the basement interface and model depths is within acceptable limits.

In addition to removing the regional anomaly, gravity effects of the higher density Lower Rainier Mesa tuffs and Area 20 lavas are stripped from the residual anomaly based on thickness estimates from borehole stratigraphic data. Average density contrasts of 400 kg/m^3 and 250 kg/m^3 are assumed for Rainier Mesa tuffs and Area 20 lavas, respectively, based on analysis of the density vs. depth plots from the borehole gravity logs (Figure 5). The gravity effects of these layers are removed using a

Begin

Fit smoothing spline to profile gravity data and interpolate at desired sample spacing.

Fit smoothing spline to gravity effects of higher density lavas and tuffs calculated along model profiles and subtract from profile observations.

Find boreholes along profile line which penetrate to the gravity basement to use as constraints for the regional anomaly calculation.

Extend model profile to include gravity stations resting on outcrop of lithology representing gravity basement for constraint of regional anomaly.

Estimate initial regional anomaly by a straight line fit of gravity stations on basement outcrops.

Subtract initial regional anomaly from observed gravity anomaly.

Execute inversion algorithm (Figure 25) to produce an initial gravity model.

Calculate residual error between borehole depths and initial model depths.

Repeat

Use residual error between borehole depths and model depths to update gravity values used in the regional anomaly calculation.

Fit a second degree polynomial by least squares to updated gravity values for new regional anomaly estimate.

Subtract regional anomaly from observed gravity anomaly.

Execute inversion algorithm (Figure 25) to produce a new gravity model.

Calculate residual error between borehole depths and model depths.

Until residual error between borehole depths and model depths is less than desired tolerance.

Interpret model.

End

Figure 33. Algorithm outlining the modeling procedure.
Several different programs are represented by this
algorithm.

77

Figure 34.   Boreholes used to constrain gravity models
A-A' and B-B' are labeled.   The outline of Silent
Canyon caldera is also indicated.
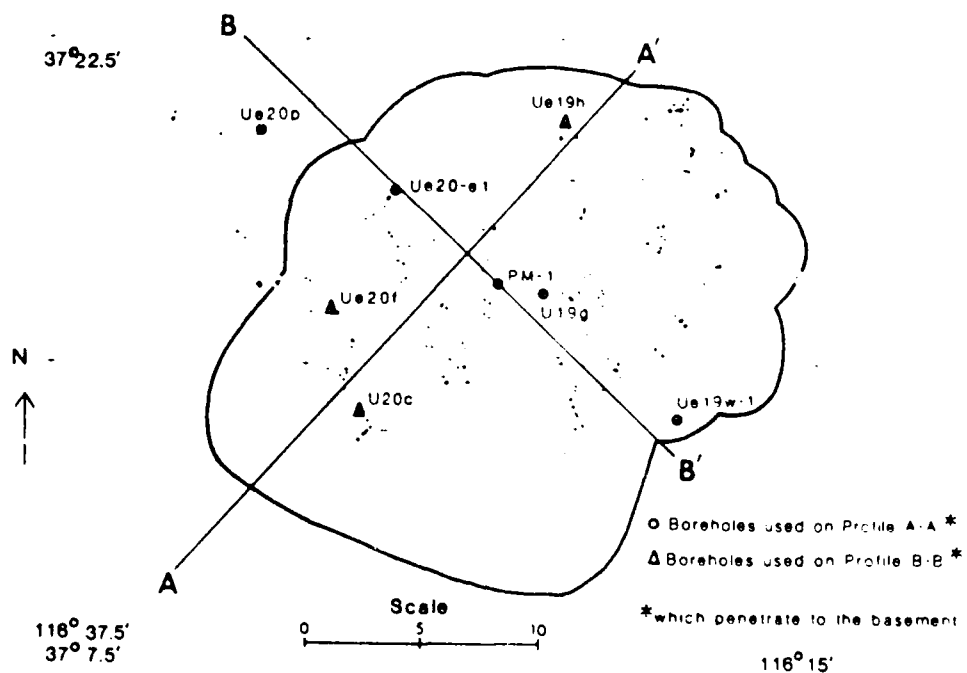
Bouguer slab approximation. The residual data are fitted with a smoothing spline (Reinsch, 1967) and interpolated at 0.5 km intervals. Approximately 57 gravity stations are used for profile B-B'.

Figure 35 is the gravity model for profile B-B'. This profile is of particular importance as it closely parallels the profile of a seismic reflection/refraction survey which was run in June, 1986 at Pahute Mesa. Least squares error of the theoretical gravity data is ± 1.27 mGals (4 percent error) with a maximum error of 6.78 mGals (21 percent error) (Figure 36). Rms error of the depth residuals is ± 0.048 km with a maximum of 0.16 km at borehole Ue20e-1. The regional anomaly is shown in Figure 37. The spectral model for profile B-B' is shown in Figure 38.

Effectiveness of the Regularization Filter:

As the results have demonstrated, application of a regularization filter stabilizes downward continuation by suppressing high wavenumber components of the data spectrum. A basic assumption of the experimental results is that the gravity anomaly was composed of sources at depth and that effects of any intervening masses are filtered out in order to stabilize the downward continuation process. If the gravity anomaly is due to contributions from a source at a single interface or depth, this assumption is valid. However, since

Figure 35. Pahute Mesa gravity model B-B'. Thicknesses of Rainier Mesa (Tmr) and Area 20 lavas (Tra) are estimated from borehole stratigraphic data.
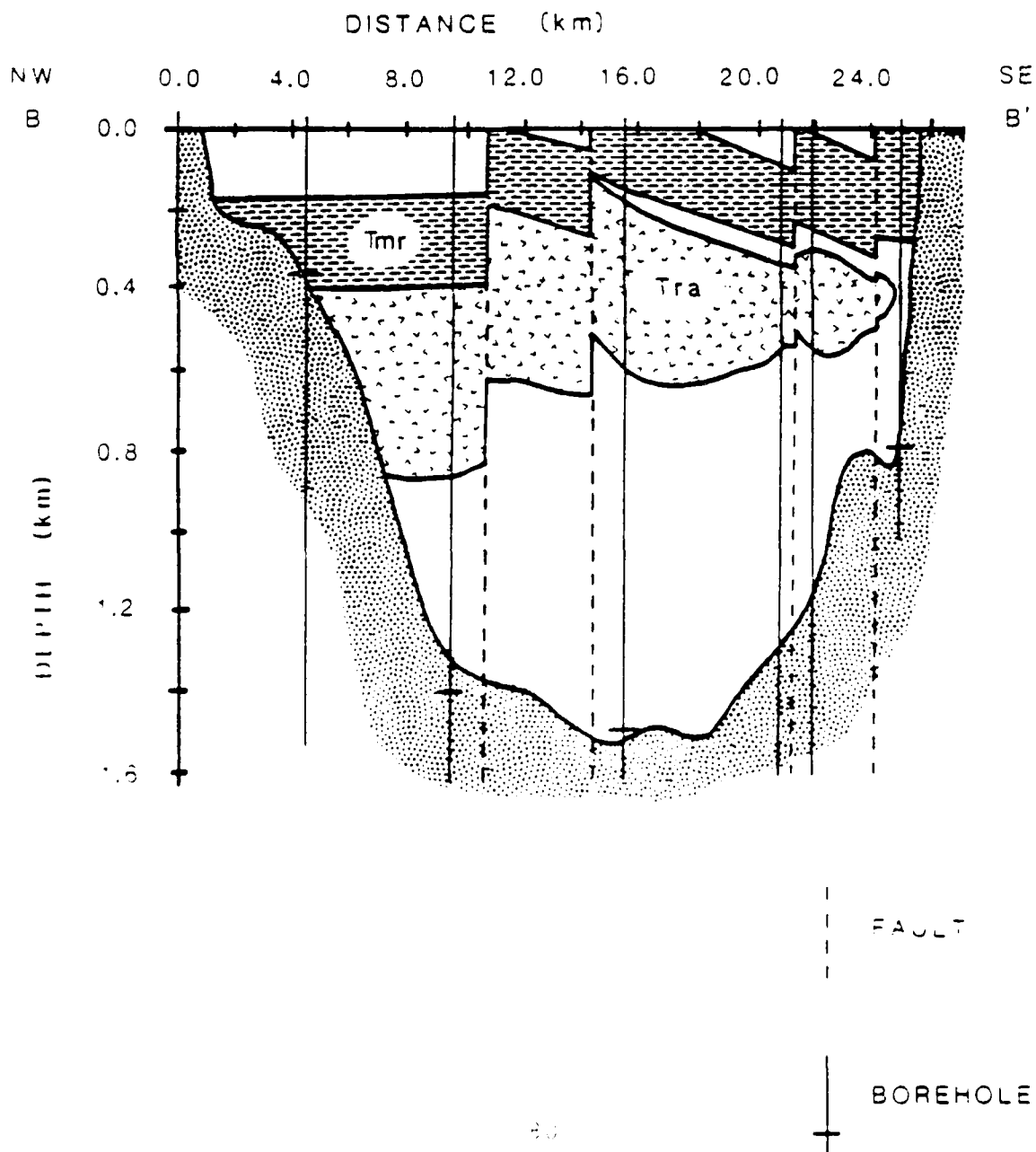
Figure 36. Observed residual gravity anomaly plotted
with gravity anomaly calculated in the modeling
procedure (Figure 33) for profile B-B'.

NW-SE PROFILE B-B'
RESIDUAL ANOMALY
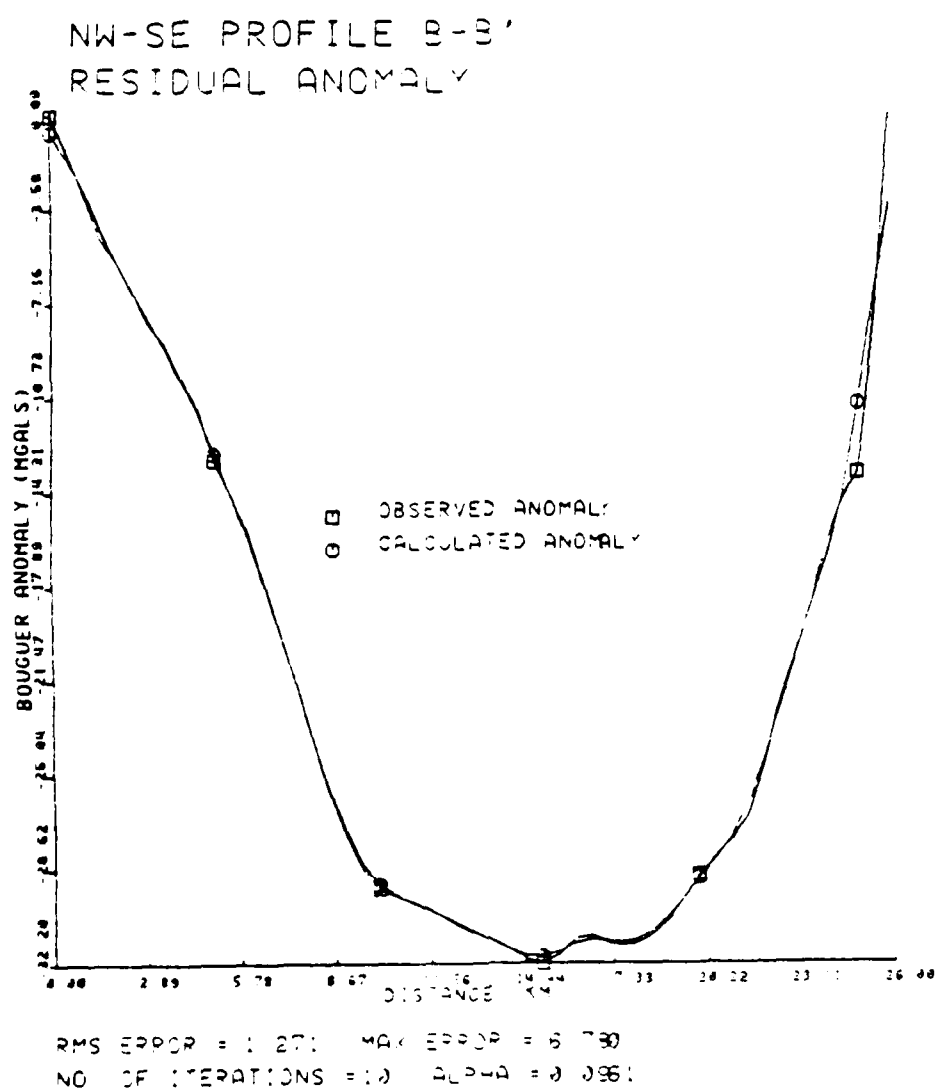
Figure 37. Observed Bouguer anomaly values for profile
B-B' plotted with the final regional anomaly. The
regional anomaly for profile B-B' is a second degree
polynomial.
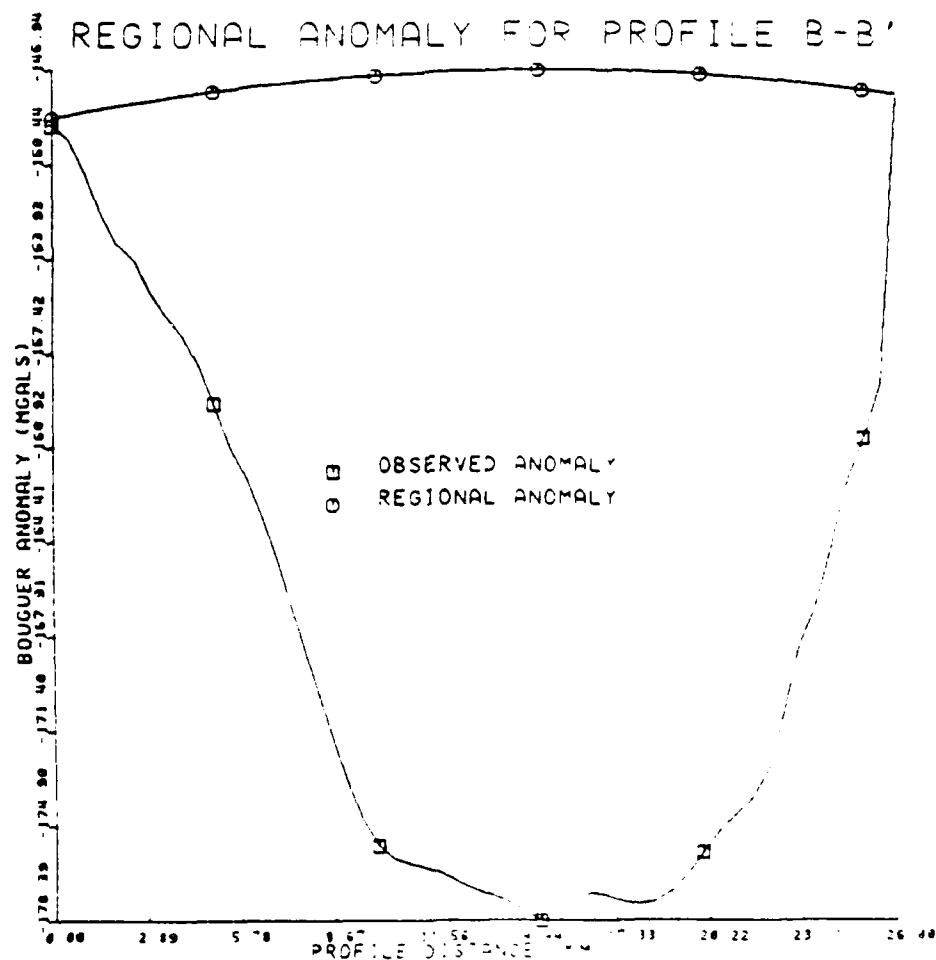
Figure 38. Spectral model for profile B-B'. Profile B-B' appears to have shallow sources which have been filtered out in addition to the noise.

CROSSOVER FREQUENCY : 185

83
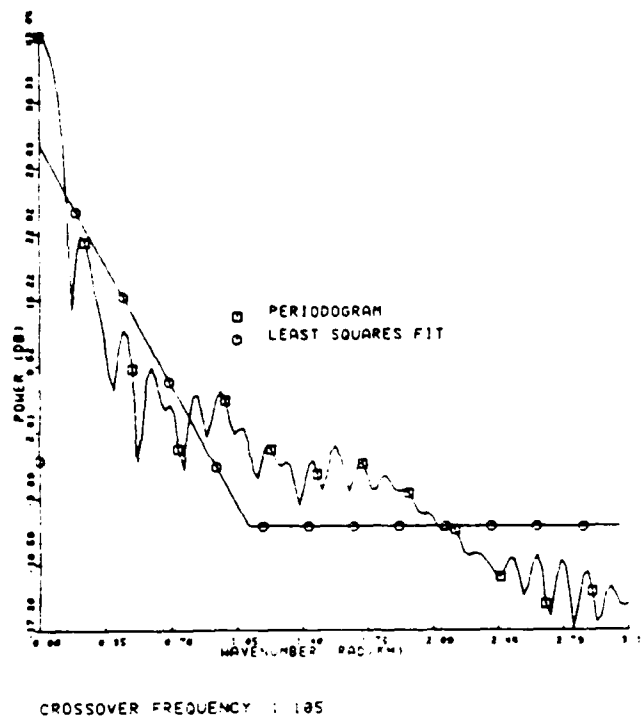
contributions to the gravity effect from shallower sources are suppressed in the filtering process, the resulting gravity model from data containing contributions from sources at different depths will not contain any information about shallower sources. For example, for Pahute Mesa gravity models, greatest data misfit for each profile occurs along the sides of the anomaly where the caldera depth shallows. This is due to suppression of high wavenumber content of the gravity data during the regularization process. An improvement to the regularization process would be to allow for non-stationary aspects of gravity data for areas such as a basin, where basement depth varies as a function of distance across the basin. This could be accomplished by assuming that the data spectrum varies smoothly over space, and spectral estimates could be made locally to accommodate changes in depth across an area (Priestly, 1981). By using a space-variable regularization filter, effects of shallow structure could be preserved and filter width used as an estimate of resolution. Covariance of the model could also be estimated from the filter function.

Effectiveness of the Vertically Varying Density Function:

Although effective at Pahute Mesa, use of a linearly varying density-depth relation has serious drawbacks which limiting the overall usefulness of such a

method. In the procedure described in Figure 33, the inverse iteration is repeated until convergence is obtained, as previously discussed. If, during execution of the procedure, model depth falls below the depth at which the value of the density function equals zero, the solution begins to diverge rapidly. Model depths could be constrained to have a lower bound set above turnover point of the density function. However, this is not a totally satisfactory solution as it biases the model with respect to the imposed constraint (Menke, 1984). For Pahute Mesa, the density function saturates at a depth of about 2.0 km, and parts of the caldera basement which are deeper than 2.0 km cannot be modeled using the density function presented in this study. Since the density function adopted is somewhat arbitary, based on a linear fit to boreholes with density information, changing the density function to accommodate deeper parts of the caldera will circumvent saturation of the density function. However, a better solution is to use the more appropriate exponential density function which allows for falloff rate and saturation of density at depth. The linear density variation of the Fourier gravity inversion method is then most useful when the density function defining the model does not change sign near the basement interface.

Estimates of covariance and resolution for non-linear inverse problems are not easily calculated since the distribution function is not usually known (Menke, 1984). In the case of the Fourier gravity inversion method with the addition of a linearly varying density vs. depth function, it is observed that resolution decreases with increasing depth as density contrast becomes smaller. Perturbations to the model at shallower depths contributes more significantly to the overall gravity effect than perturbations at greater depths. Weighting least squares error calculations as a function of depth could compensate for this lack of resolution. Also, as the regularization filter suppresses effects of shallower sources, model resolution at greater depths is decreased in order to decrease model variance.

Another problem with the Fourier gravity inversion technique is the tendency for model depths along profile edges to become negative, which is a result of overfiltering along the flanks of the caldera, as discussed previously. Because of the steep gravity gradient along profile edges, the loss of information from regularization results in a lack of continuity along the profile edges. According to Dugue's Theorem, the Fourier transform of a continuous, positive definite function is uniformly convergent; however, since the discrete representation of positive definite functions

are generally not continuous at the endpoints, uniform convergence is not assured (Schmetterer, 1965).

Interpretation of Pahute Mesa Depth Models:

Choice of the inverse Fourier modeling technique for Pahute Mesa is made based on the assumption that fluctuations in the gravity anomaly are caused by variations in the source topography. Suppression of shallower source effects is desirable to decrease model variance. However, since the assumption is also made to model Silent Canyon Caldera as a basin-type structure, inclusion of a space-variable, regularization filter would increase model resolution along the edges of the caldera where signficant structural changes are apparent and the overfiltering in this study occurs.

For example, in the gravity model for profile B-B', the most significant mismatch between observed and calculated anomalies is toward the southeastern profile edge at a depth of about 0.9 km. This shallow structure coincides with a mapped surface fault, the Scrugham Peak fault, (Orkild et al., 1969) which appears from this model to extend into the basement. The spectral model for profile B-B' indicates the presence of at least one and possibly two shallow sources. The poor least squares fit to the periodogram results in larger maximum error between the residual anomalies as high wavenumber content of the anomaly corresponding to shallower structure is

87

filtered out. Model resolution and variance for this profile can be improved by use of a space variable, regularization filter.

Profile B-B' is well constrained by boreholes (Figure 34), indicating that basement depths are probably good to within the least squares residual error between model and borehole depths. Also, the good distribution of boreholes provides better control on thicknesses of higher density units stripped from profile data. Because of the abundance of normal faulting at Pahute Mesa, thickness of the higher density units varies considerably in some places.

Profile B-B' does not transect the center of gravity low; however, undulations in the deepest part of the model for B-B' suggest some structural complexity in basement topography of the caldera. A three-dimensional model of Pahute Mesa data could resolve some of these questions.

The shape of the second degree polynomial regional anomaly subtracted from each profile, a regional high indicating a positive density contrast, may indicate an intrusive source at depth. The existence of a large intrusive body has been suggested by Snyder and Carr (1984) in a study area southwest of Timber Mountain based on aeromagnetic, borehole, heat flow and gravity data. Spence (1974) postulated the existence of a high velocity

zone in the upper mantle beneath Silent Canyon caldera from analysis of teleseismic P-wave residuals. If this zone of high velocity corresponds to a crustal or upper mantle magma body as suggested by Spence, then the gravity data should exhibit an associated low order, long wavelength gravity high unless it is isostatically compensated.

The Wide Angle Seismic Survey

In the specification of a geophysical model at Pahute Mesa the borehole data are limited in depth extent and coverage and the gravity models lack resolution at depth and are not directly sensitive to seismic velocity. Direct seismic observation of the caldera structure would be of considerable importance to the creation of a geophysical model. The presence of local, thin, high velocity layers (such as the Rainer Mesa tuff) and a very low Q in the near surface materials (perhaps as low as 30) make conventional seismic reflection surveys impractical. With a plan based on some preliminary hypotheses concerning the caldera structure, an unconventional, wide angle seismic survey has been performed. In addition to the geophysical constraints the presence of archeological sites on Pahute Mesa limit the possible location of shot holes.

Geologic and gravity models suggest that the Silent Canyon caldera can be thought of as a basin founded on older, less porous, peralkaline volcanics associated with the caldera collapse (termed "basement" in this report). The basin is filled with low density, high porosity tuffs and higher density lava and tuff flows from sources to the south and west. The basement rocks outcrop to the southeast of Pahute Mesa. The caldera margin could be steeply faulted or more gently slumped with large zones

of brecciation. Several major north-south trending faults cut through the area and have been active during much of the volcanic deposition. A major northwest trending structure may also be present.

A joint program for the execution of a seismic experiment was developed between UTD and Los Alamos in 1985 and 1986. Richard Warren and Allen Cogbill of the Earth and Space Sciences Division at Los Alamos were active in the planning of the experiment. Los Alamos provided field support at NTS, field personnel, some equipment and shot hole drilling. Ed Criley of the USGS at Menlo Park, CA was subcontracted to acquire and handle the explosives. Based on the considerations discussed above the program illustrated in Figure 39 was laid out in the Spring of 1986. A single shot point was located on outcropping basement volcanics in Big Burn Valley southeast of Pahute Mesa. A line of recording sites was drawn along available roads on the Mesa above and trending toward the hole PM-1. This hole is one of the deepest drilled at Pahute Mesa and is a logical place to tie the end of the line. The line is close to several other boreholes providing stratigraphic and velocity control. The hole U19w is of particular interest as it appears to be near the caldera margin. Both the caldera margin (as indicated on Orkild et al., 1969) and the north-south trending faults are crossed at a favorable

91

Figure 39.   This map shows the layout of the 1986 seismic survey at Pahute Mesa, Nevada. The "Y" symbols indicate geophone group locations and the triangles indicate Dinoseis shot points.

PAHUTE MESA SEISMIC SURVEY 1986
SCALE 1: 128000
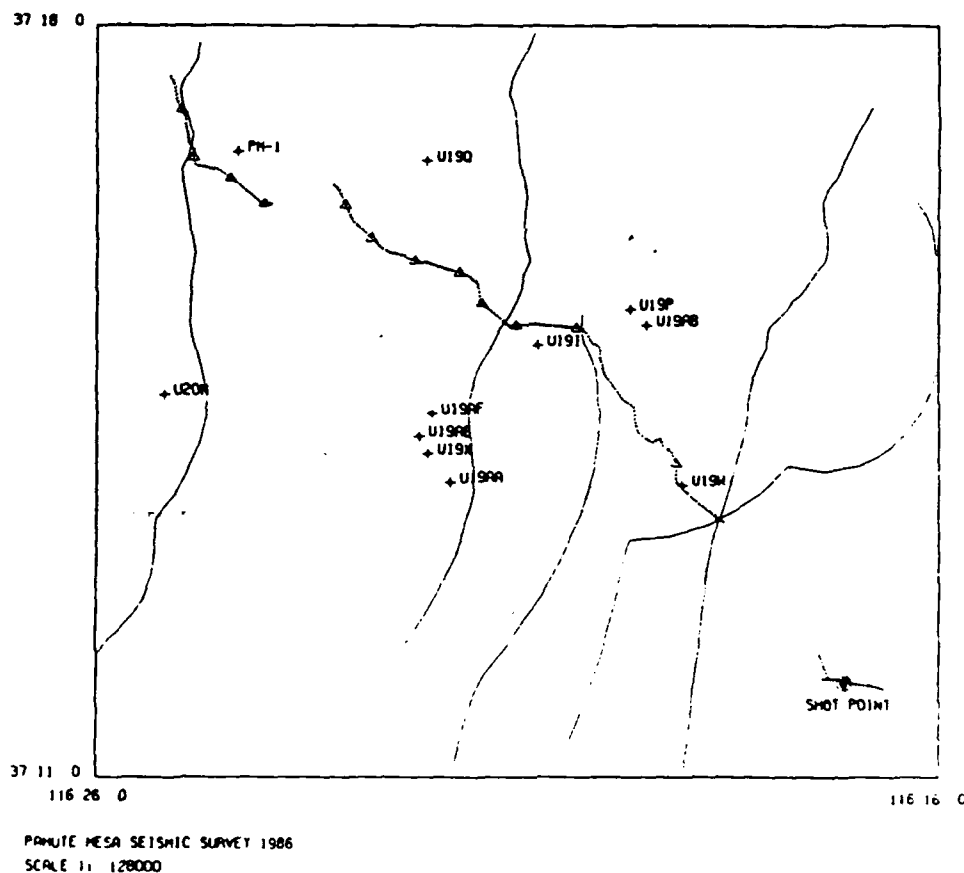
angle by the line. The profile is unreversed by shots at the northwestern end of the line and major lateral structural variations occur along the line. The intent is to inject seismic energy directly into the basement and observe refracted and reflected waves from the basement after propagation through the post caldera structure above. The interpretation of undershot structures similar to this was successful at Crater Flat to the south of this area (Hoffman and Mooney, 1984). The interpretation will rely on geologic and gravity models to insure some measure of uniqueness. One goal of this experiment is to demonstrate that useful seismic data can be acquired at Pahute Mesa. If this turns out to be the case, future experiments will certainly be planned with more complete shot point distributions.

The recording line is 12.5 km long with a 3.5 km offset from the shot point, necessitated by topography. Twenty four channel spreads of 1.5 km aperture and 67 m group interval were deployed. Each channel recorded a string of six 4.5 Hz geophones spaced 3 to 6 m apart. A Geometrics ES-2420 recording system was used for 15 bit floating point digital records on nine track tape. A 2 msec sample interval was used. The spreads were shot to the Big Burn Valley shot point and also from east with a 12 liter Dinoseis (ARCO trademark) and est The spreads recording the explosive shots e
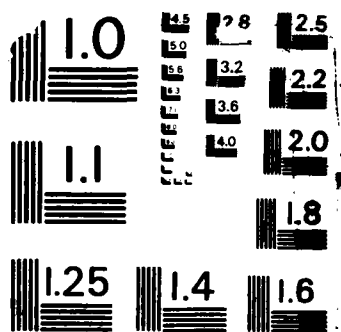
MICROCOPY RESOLUTION TEST CHART

NATIONAL BUREAU OF STANDARDS-1963-A

Table 3

Flag #'s: S_i = flag locations near the HE-shot point (Big Burn Valley)
            All other flag #'s represent locations on Pahute Mesa

SP = flag # of shotpoint

NEAR OFFSET = offset from high explosive shotpoint in Big Burn Valley

NVSS = # of vertically summed shots yielding this record

FILL TM = fill time of Dinoseis guns in seconds

DEPTH = depth of high-explosive shots

TIME = local daylight savings time (PDT)

SHOT	DATE (m-d)	TIME	FLAG #'S	SP	NVSS	# OF GUNS & FILL TM	REMARKS
1	6-3	10:21	S1 - S24	1	6		These five
2	6-3	10:28:48	S1 - S24	1	5		shots are
3	6-3	10:46:17	S1 - S24	8	5		located near the
4	6-3	11:05:47	S1 - S24	16	5		high-explosive
5	6-3	11:29:49	S1 - S24	24	5		shotholes
1	6-6	08:41:54	1 - 24	8	5	1g 2sf	Source is 30 ft NE of 8
2	6-6	09:40:28	13 - 36	13	3	1g 2sf	" " 50 ft E of 13
3	6-6	09:44:18	1 - 24	13	3	1g 2sf	" " " " " " "
4	6-6	10:43:53	1 - 24	22	6	2g 2sf	
5	6-6	10:58:12	22 - 45	22	6	2g 2sf	
6	6-7	08:48:51	47 - 70	70	6	2g 2sf	
7	6-7	09:01:05	59 - 82	70	6	2g 2sf	Channel 24 is bad
8	6-7	09:04:34	70 - 93	70	6	2g 2sf	
9	6-7	20:07:34	73 - 96	86	6	2g 2sf	Channels 16-24 noisy
10	6-7	20:11:55	86 - 109	86	6	2g 2sf	
11	6-7	20:30:03	73 - 96	97	6	2g 2sf	
12	6-7	20:34:36	97 - 120	97	6	2g 2sf	Channels 23,24 noisy
13	6-8	06:50:49	85 - 108	108	9	2g 3sf	Channel 4 is noisy
14	6-8	19:08:06	109 - 132	108	16	2g 3sf	
15	6-8	19:55:19	109 - 132	120	8	2g 4sf	Source is 65 ft SE of 120
16	6-8	20:12:38	121 - 144	120	9	2g 4sf	" " " " " " "
17	6-8	20:28:45	121 - 144	133	6	2g 3sf	
18	6-9	05:53:49	121 - 144	144	9	2g 2sf	
19	6-9	06:43:12	171 - 194	171	9	2g 2sf	
20	6-9	19:06:42	195 - 218	194	16	2g 3sf	No data last 2 tr.
21	6-9	20:07:42	171 - 194	182	9	2g 3sf	
22	6-9	20:24:33	171 - 194	194	16	2g 3sf	
23	6-9	20:37:13	193 - 216	207	6	2g 3s	Source is 30 ft S of 207

Table 3

SHOT	DATE (m-d)	TIME	FLAG #'S	SP	NEAR OFFSET [km]	CHARGE WT. [lbs]	[kg]	DEPTH [ft]	[m]	REMARKS
1	6-5	17:11:21	1 - 24	4	3.470	30.0	13.6	50.0	15.2	Channel 11 is dead
2	6-5	17:35:57	1 - 24	4	3.470	30.0	13.6	40.0	12.2	" " " "
3	6-5	18:01:46	25 - 48	3	5.021	60.0	27.2	50.0	15.2	" " " "
4	6-6	08:11:43	13 - 36	3	4.246	30.0	13.6	47.0	14.3	Bad rec.
5	6-6	08:50:01	13 - 36	2	4.246	60.0	27.2	51.0	15.5	
6	6-6	09:50:27	1 - 24	3	3.470	60.0	27.2	44.0	13.4	
7	6-6	10:09:45	25 - 48	5	5.021	60.0	27.2	50.0	15.2	
8	6-6	17:20	37 - 60	6	5.755	60.0	27.2	50.0	15.2	Shots 8 & 9 were not
9	6-6	17:40	48 - 71	9	6.260	120.0	54.4	55.0	16.8	recorded on the tape
10	6-6	18:08:53	48 - 71	10	6.260	90.0	40.8	55.0	16.8	Very noisy
10	6-6	18:09:32	48 - 71	10	6.260	90.0	40.8	55.0	16.8	Duplicate rec. on tape
11	6-7	07:13:39	37 - 60	11	5.755	150.0	68.0	55.0	16.8	Bad rec.
12	6-7	07:36:55	37 - 60	8	5.755	210.0	95.3	56.0	17.1	
13	6-7	08:21:03	48 - 71	1	6.260	210.0	95.3	66.0	20.1	Channel 22 is noisy
14	6-7	09:14:23	61 - 84	7	7.201	210.0	95.3	66.0	20.1	
15	6-7	18:57:08	73 - 96	15	7.814	300.0	136.1	65.0	19.8	Channel 6 is noisy
16	6-7	19:12:44	97 - 120	14	9.102	480.0	217.7	65.0	19.8	
17	6-7	19:46:02	85 - 108	13	8.409	390.0	176.9	65.0	19.8	Channel 6 is noisy
18	6-8	19:24:36	109 - 132	17	9.782	540.0	244.9	76.0	23.2	
19	6-8	19:42:05	121 - 144	16	10.507	720.0	326.6	75.0	22.9	
20	6-9	07:18:18	171 - 194	12	13.140	1020.0	462.7	75.0	22.9	
21	6-9	19:49:08	193 - 216	18	14.530	1500.0	680.4	80.0	24.4	Channel 17 is bad

Figure 40. The data from the 1986 seismic survey is shown in record section form. The data have been lowpass filtered at 25 Hz and redundant traces editted. A reduction velocity of 4.6 km/sec has been used. The topographic profile has a vertical exaggeration of two times. The travel times for the first arrivals from the Dinoseis shots are also plotted.

Pahute Mesa Seismic Line

Radial Distance (km)

Time - Dist/4.60 (sec)
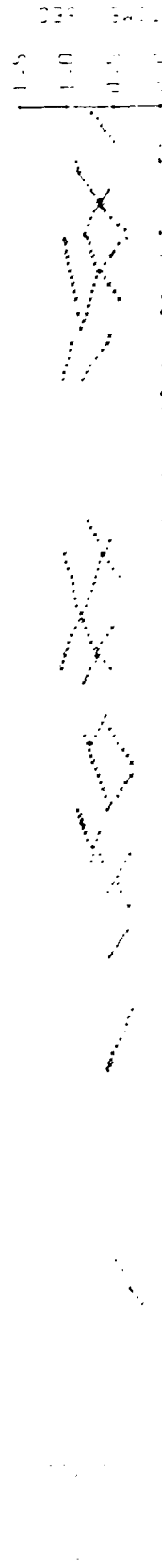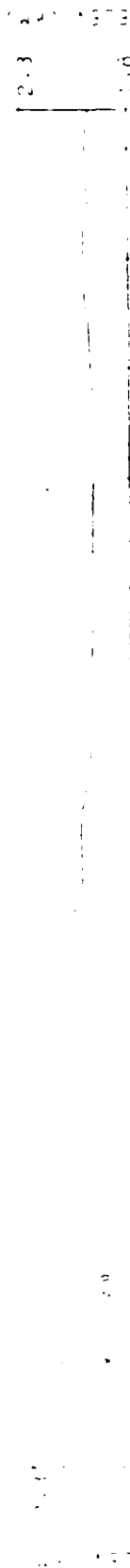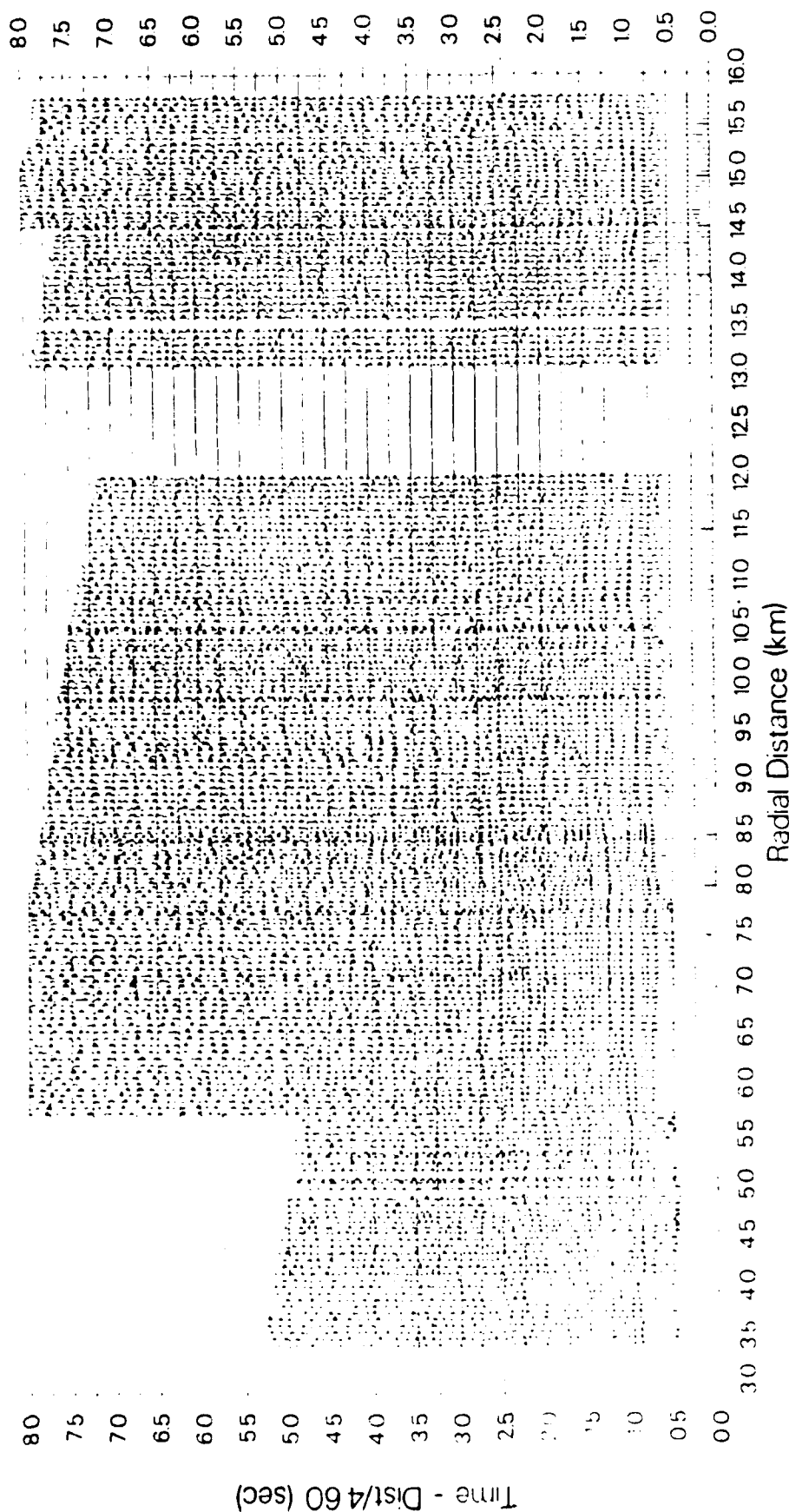
for the first arrivals quite well. Future interpretation efforts will start with geologic and geophysical cross sections developed from borehole information. A computer program based on the psuedospectral approximation for the acoustic and elastic wave equations (Kosloff and Baysal, 1982 and Kosloff et al., 1984) will be used to model the seismic wave field produced by this experiment. The resulting cross section should agree with the boreholes, gravity data and the seismic section, and hence should be an accurate representation of the caldera structure across its southeast margin. The model should predict the seismic response of nuclear tests located near the profile.

Acknowledgments

This project, with its extensive field work, required the efforts and support of many people. The authors of this report would like to acknowledge some of the most helpful. Our co-workers at UTD: Carlos Aiken, Joe Nation, Vicky Rouse, Russell Heidesch, David Hersey, Beth Ullom, Dennis Harry, Richard Jenkins, Kevin Mickus, Russell Kojima and Bob Schellhorn. At Los Alamos and NTS: Allen Cogbill, Richard Warren, Don Collins, Frank Byers, Jack House, Wayne Meadows and Fred Holmuth. Paul Orkild, Don Healy, Ed Criley and Jeff Wynn of the U. S. Geological Survey.

Appendix

Derivation of the Fourier gravity inversion solution with density a linear function of depth:

Starting with the expression for the gravitational potential due to attraction from a layer of material:

$$U(r_0) = G \int_V \sigma(z) / |r_0 - r| \quad dV$$

where:

$$G = \text{gravitational constant}$$

$$V = \text{volume}$$

$$\sigma(z) = \text{linear density function}$$

$$\sigma(z) = \sigma_0 + cz$$

$$r_0 = \text{position of the observation}$$

$$r = \text{position within V}$$

$$\underline{r} = \text{projection of r onto the surface } z = 0.$$

and expanding the integral expression,

$$U(r_0) = G \int_D \int_0^{h(\underline{r})} \sigma(z) / |r_0 - r| \quad dz \; dS$$

Taking the Fourier transform of the gravitational potential, the expression becomes:

$$F[U(r_0)] = \int_X U(r_0) \exp(i\underline{k}\cdot\underline{r}) \quad dS_0$$

$$F[U(r_0)] = G \int_D \int_0^{h(\underline{r})} \exp(i|\underline{k}| \; (r_0 - r)) \exp(i\underline{k}\cdot\underline{r}) \; dz \; dS_0$$

101

Transforming to polar coordinates:

$$F[U(r_0)] = G \int_D \int_0^{h(\underline{r})} 2\pi \, \sigma(z) \, \exp(i\underline{k}\cdot\underline{r})$$

$$\cdot \, J_0(|\underline{k}|R) \, / \, (R^2 + A^2)^{1/2} \, R \quad dz \, dR$$

where:

$$R \quad = \quad ((x-x_0)^2 + (y-y_0)^2)$$

$$A \quad = \quad (z-z_0)$$

By use of a Hankel transform (Bracewell, 1965), this reduces to:

$$F[U(r_0)] = 2\pi \, G \int_D \int_0^{h(\underline{r})} \sigma(z) \, \exp(|\underline{k}| \, (z_0 - z))$$

$$\cdot \, \exp(i|\underline{k}|\underline{r}) \, / \, |\underline{k}|$$

After rearranging terms:

$$F[U(r_0)] = 2\pi \, G \int_D \int_0^{h(\underline{r})} \sigma(z) \, \exp(i|\underline{k}|\underline{r} - |\underline{k}|z_0)$$

$$\cdot \, \exp(|\underline{k}|z) \, / \, |\underline{k}| \quad dz \, dS$$

and substituting in the function $\sigma(z)$:

$$F[U(r_0)] = 2\pi \, G \int_D \int_0^{h(\underline{r})} (\sigma_0 + cz) \, \exp(i|\underline{k}|\underline{r} - |\underline{k}|z_0)$$

$$\cdot \, \exp(|\underline{k}|z) \, / \, |\underline{k}| \quad dz \, dS$$

Solving the depth integral analytically results in:

$$F[U(r_0)] = 2\pi \, G \int_D \exp(i|k|r) \, \exp(-|k|z_0)$$

$$\cdot \, (\sigma_0(\exp(|\underline{k}|h(\underline{r})) - 1) \, / \, |\underline{k}| + c((|\underline{k}|h(\underline{r}) - 1)$$

$$\cdot \, \exp(|\underline{k}|h(\underline{r})) + 1) \, / \, |\underline{k}|^2) \quad dS$$

After Taylor series expansion of the exponential and rear anging terms:

$$F[U(r_0)] = 2\pi\ G\ \exp(-|\underline{k}|z_0)\ (\sigma_0 \sum_{n=1}^{\infty} |\underline{k}|^{n-2}\ /\ n!\ F[h^n(\underline{r})]$$

$$+\ c \sum_{n=2}^{\infty} |\underline{k}|^{n-3}\ /\ n!\ (n-1)\ F[h^n(\underline{r})]\}$$

To include both an upper and lower surface, this expression becomes:

$$F[U(r_0)] = 2\pi\ G\ \exp(-|\underline{k}|z_0)\ (\sigma_0 \sum_{n=1}^{\infty} |\underline{k}|^{n-2}\ /\ n!\ F[h^n(\underline{r})]$$

$$-\ g^n(\underline{r})]\ +\ c \sum_{n=2}^{\infty} |\underline{k}|^{n-3}\ /\ n!\ (n-1)\ F[h^n(\underline{r})]$$

$$-\ g^n(\underline{r})]\}$$

To obtain the expression for the gravity effect, differentiate both sides with respect to z and evaluate at z_0:

$$F[\delta g(\underline{r})] = 2\pi\ G\ \exp(-|\underline{k}|z_0)\ (\sigma_0 \sum_{n=1}^{\infty} |\underline{k}|^{n-1}\ /\ n!\ F[h^n(\underline{r})]$$

$$-\ g^n(\underline{r})]\ +\ c \sum_{n=2}^{\infty} |\underline{k}|^{n-2}\ /\ n!\ (n-1)\ F[h^n(\underline{r})]$$

$$-\ g^n(\underline{r})]\}$$

To obtain the inverse expression, solve for the first term of the first infinite series as follows:

$$F[\delta g(\underline{r})] = 2\pi\ G\ \exp(-|\underline{k}|z_0)\ \sigma_0\ F[h^n(\underline{r})\ -\ g^n(\underline{r})]$$

103

$$+ \ 2\pi \ G \ \exp(-|\underline{k}|z_0) \ \{ \sigma_0 \sum_{n=2}^{\infty} |\underline{k}|^{n-1} \ / \ n! \ F[h^n(\underline{r})$$

$$- \ g^n(\underline{r})] + c \sum_{n=2}^{\infty} |\underline{k}|^{n-2} \ / \ n! \ (n - 1) \ F[h^n(\underline{r})$$

$$- \ g^n(\underline{r})]\}$$

$$F[h^n(\underline{r}) - g^n(\underline{r})] = F[\delta g(\underline{r})] \ \exp(|\underline{k}|z_0) \ / \ (2\pi \ G \ \sigma_0)$$

$$- \ \{ \sum_{n=2}^{\infty} |\underline{k}|^{n-1} \ / \ n! \ + \ (c \ / \ \sigma_0) \sum_{n=2}^{\infty} |\underline{k}|^{n-2} \ / \ n!$$

$$\cdot \ (n - 1)\} \ F[h^n(\underline{r}) - g^n(\underline{r})]$$

References

Aki, K. and Larner, K., 1970, Surface motion of a layered medium having an irregular interface due to incident plane SH waves: J. Geophys. Res., 75, 933-954.

Bracewell, R.N., 1978, The Fourier transform and its applications: McGraw Hill, Inc.

Byers, Jr., F. M., Carr, W. J., Orkild, P. P., Quinlivan, W. D. and Sargent, K. A., 1976, Volcanic suites and related cauldrons of Timber Mountain-Oasis Valley caldera complex, southern Nevada: U.S. Geol. Surv. Prof. Paper 919.

Christiansen, R. L., Lipman, P. W., Carr, W. J., Byers, Jr., F. M., Orkild, P. P. and Sargent, K. A., 1977, The Timber Mountain-Oasis Valley caldera complex of southern Nevada: Geol. Soc. Am. Bull., 88, 943-959.

Corbato, C. E., 1965, A least squares procedure for gravity interpretation: Geophysics, 30, 228-233.

Eckel, E. B., Ed., 1968, Geol. Soc. Am. Memoir 110, Nevada Test Site: Geol. Soc. Am.

Ferguson, J. F., 1987, Body wave magnitude variation at Yucca Flat, Nevada, Bull. Seis. Soc. Am., in press.

Ferguson, J. F., Felch, R. N., Aiken, C. L. V., Oldow, J. S. and Dockery, H., 1988, Models of the Bouguer gravity and geologic structure at Yucca Flat, Nevada: Geophys., 53, in press.

Forsythe G.E., Malcolm M.A. and Moler C.B., 1977, Computer methods for mathematical computations: Prentice Hall, Inc.

Gardner, G. H. F., Gardner and L. W., Gregory, A. R., 1974, Formation velocity and density - the diagnostic basics for stratigraphic traps: Geophys., 39, 770-780.

Hahn, A., Kind, E. G. and Mishra, D. C., 1976, Depth estimation of magnetic sources by means of Fourier amplitude spectra: Geophys. Prospecting, 24, 287-308.

Hammer, S., 1939, Terrain corrections for gravimeter stations: Geophysics, 4, 184-194.

Healey, D. L., 1968, Application of gravity data to geologic problems at Nevada Test Site, in Eckel, E. B., Ed., Geol. Soc. Am. Memoir 110, Nevada Test Site: Geol. Soc. Am., 147-156.

Hearst, J. R., Carlson, R. C., 1982, Measurement and analysis of gravity in boreholes, in Developments in Geophysical Exploration Methods - 3, Fitch, A. A., Ed.: Applied Science, New York.

Helmberger, D. V., Engen, G. and Grand, S., 1985, Notes on wave propagation in laterally varying structure: J. Geophys., 58, 82-91.

Hoffman, L. R. and Mooney, W. D., 1984, A seismic study of Yucca Mountain and vicinity, southern Nevada; data report and preliminary results: U. S. Geol. Surv., Open File Rept. 83-588, Menlo Park, CA.

Ibrahim, A. W. and Keller, G. V., 1981, Seismic velocities and electrical resistivity of recent volcanics and their dependence on porosity, temperature, and water staturation: Geophys., 46, 1415-1422.

Kelley, K. R., Ward, R. W., Treitel, S. and Alford, R. M., 1976, Synthetic seismograms, a finite difference approach: Geophys., 41, 2-27.

Kistler, R. W., 1968, Potassium-Argon ages of volcanic rocks in Nye and Esmeralda Counties, Nevada, in Eckel, E. B., ed., Nevada Test Site: Geol. Soc. Am. Mem. 110, 251-262.

Korvin, G., 1984, Shale compaction and statistical physics: Gephys. J. R. astr. Soc., 78, 35-50.

Kosloff, D. and Baysal, E., 1982, Forward modeling by a Fourier method, Geophys., 47, 1402-1412.

Kosloff, D., Reshef, M. and Loewenthal, D., 1984, Elastic wave calculations by the Fourier method: Bull. Seis. Soc. Am., 74, 875-891.

Leonard, M. A. and Johnson, L. R., 1987, Velocity structure of Silent Canyon caldera, Nevada Test Site: Bull. Seis. Soc. Am., 77, 597-613.

Lynnes, C. and Lay, T., 1984, Defocusing of short period P waves by a high velocity anomaly beneath Pahute Mesa, abst.: EOS, Trans. Am. Geophys. Union, 65, 994.

Marvin, R. F., Byers, Jr., F. M., Mehnert, H. H., Orkild, P. P. and Stern, T. W., 1970, Radiometric ages and stratigraphic sequence of volcanic and plutonic rocks, southern Nye and western Lincoln Counties, Nevada: Geol. Soc. Am. Bull., 81, 2657-2676.

McLaughlin, K. L., Anderson, L. M. and Lees, A. C., 1987, Effects of local geologic structure on Yucca Flats, Nevada Test Site, explosion waveforms: two-dimensional linear finite-difference simulations: Bull. Seis. Soc. Am., 77, 1211-1222.

Menke, W., 1984, Geophysical data analysis: discrete inverse theory: Academic Press, Inc.

Minster, J. B., Savino, J. M., Rodi, W. L., Jordan, T. H. and Masso, J. F., 1981, Three-dimensional velocity structure of the crust and upper mantle beneath the Nevada Test Site: Systems, Science and Software rept. SSS-R-81-5138.

Nelder, J. A. and Mead, R., 1965, A simplex method for function minimization: Comp. J., 7, 308-313.

Nettleton, L. L., 1976, Gravity and magnetics in oil prospecting: McGraw-Hill, Inc.

Noble, D. C., Sargent, K. A., Mehnert, H. H., Ekren, E. B. and Byers, Jr., F. M., 1968, Silent Canyon volcanic center, in Eckel, E. B., Ed.: Geol. Soc. Am. Memoir 110, Nevada Test Site: Geol. Soc. Am., 65-76.

Oldenburg, D. W., 1974, The inversion and interpretation of gravity anomalies: Geophysics, 39, 526-536.

Orkild, P. P., Byers, Jr., F. M., Hoover, D. L. and Sargent, K. A., 1968, Subsurface geology of Silent Canyon caldera, Nevada Test Site, Nevada, in Eckel, E. B., Ed., Geol. Soc. Am. Memoir 110, Nevada Test Site: Geol. Soc. Am., 77-86.

Orkild, P .P., Sargent, K. A. and Snyder, R. P., 1969, Geologic map of Pahute Mesa, Nevada Test Site, Nye County, Nevada: U.S. Geol. Surv. Misc. Geol. Inv. Map I-567.

Parker, R. L., 1972, The rapid calculation of potential anomalies: Geophys. J. R. astr. Soc., 31, 447-455.

Plouff, D., 1977, Preliminary documentation for Fortran program to compute gravity terrain corrections based on topography digitized on a geographic grid: U.S. Geol. Surv. Open File Report 77-535.

Priestley, M. B., 1981, Spectral analysis and time series: Academic Press, Inc.

Reinsch, C. H., 1967, Smoothing by spline functions: Numerische mathematik, 10, 177-183.

Schmetterer, L., 1965, Some theorems on the Fourier analysis of positive definite functions: Proc. Amer. Math. Soc., 16, 1141-1146.

Snyder, D.and Carr, W. J., 1984, Interpretation of gravity data in a complex volcano-tectonic setting, southwestern Nevada: J. Geophys. Res., 89, 10193-10206.

Spector, A. and Grant, F. S., 1970, Statistical models for interpreting aeromagnetic data: Geophysics, 35, 293-302.

Spence, W., 1974, P-wave residual differences and inferences on an upper mantle source for the Silent Canyon volcanic centre, southern Great Basin, Nevada: Geophys. J. R. astr. Soc., 38, 505-523.

Taylor, S. R., 1983, Three-dimensional crust and upper mantle structure at the Nevada Test Site: J. Geophys. Res., 88, 2220-2232.

Tikhonov, A. N., Glasko, V. B., Litvinenko, O. R. and Melikhov, V. P., 1968, Analytic continuation of a potential in the direction of disturbing masses by the regularization method: Izv., Earth Physics, 12, 30-48.

Warren, R. G., Byers, Jr., F. M. and Orkild, P. P., 1985, Post-Silent Canyon caldera structural setting for Pahute Mesa: Proc. 3rd Symposium on Containment of Underground Nuclear Explosions, 2, 3-30.

Professor Keiiti Aki
Center for Earth Sciences
University of Southern California
University Park
Los Angeles, CA 90089-0741

Professor Charles B. Archambeau
Cooperative Institute for Resch
  in Environmental Sciences
University of Colorado
Boulder, CO   80309

Dr. Thomas C. Bache Jr.
Science Applications Int'l Corp.
10210 Campus Point Drive
San Diego, CA 92121   (2 copies)

Dr. Douglas R. Baumgardt
Signal Analysis & Systems Div.
ENSCO, Inc.
5400 Port Royal Road
Springfield, VA 22151-2388

Dr. S. Bratt
Science Applications Int'l Corp.
10210 Campus Point Drive
San Diego, CA 92121

Dr. Lawrence J. Burdick
Woodward-Clyde Consultants
P.O. Box 93245
Pasadena, CA 91109-3245 (2 copies)

Professor Robert W. Clayton
Seismological Laboratory/Div. of
  Geological & Planetary Sciences
California Institute of Technology
Pasadena, CA 91125

Dr. Vernon F. Cormier
Department of Geology & Geophysics
U-45, Room 207
The University of Conneticut
Storrs, Connecticut 06268

Dr. Zoltan A. Der
ENSCO, Inc.
5400 Port Royal Road
Springfield, VA 22151-2388

Professor John Ferguson
Center for Lithospheric Studies
The University of Texas at Dallas
P.O. Box 830688
Richardson, TX 75083-0688

Professor Stanley Flatte'
Applied Sciences Building
University of California, Santa Cruz
Santa Cruz, CA 95064

Professor Steven Grand
Department of Geology
245 Natural History Building
1301 West Green Street
Urbana, IL 61801

Professor Roy Greenfield
Geosciences Department
403 Deike Building
The Pennsylvania State University
University Park, PA 16802

Professor David G. Harkrider
Seismological Laboratory
Div of Geological & Planetary Sciences
California Institute of Technology
Pasadena, CA 91125

Professor Donald V. Helmberger
Seismological Laboratory
Div of Geological & Planetary Sciences
California Institute of Technology
Pasadena, CA 91125

Professor Eugene Herrin
Institute for the Study of Earth
 & Man/Geophysical Laboratory
Southern Methodist University
Dallas, TX 75275

Professor Robert B. Herrmann
Department of Earth & Atmospheric
      Sciences
Saint Louis University
Saint Louis, MO 63156

Professor Lane R. Johnson
Seismographic Station
University of California
Berkeley, CA 94720

Professor Thomas H. Jordan
Department of Earth, Atmospheric
 and Planetary Sciences
Mass Institute of Technology
Cambridge, MA 02139

Dr. Alan Kafka
Department of Geology &
  Geophysics
Boston College
Chestnut Hill, MA 02167.

Professor Leon Knopoff
University of California
Institute of Geophysics
  & Planetary Physics
Los Angeles, CA 90024

Professor Charles A. Langston
Geosciences Department
403 Deike Building
The Pennsylvania State University
University Park, PA 16802

Professor Thorne Lay
Department of Geological Sciences
1006 C.C. Little Building
University of Michigan
Ann Harbor, MI 48109-1063

Dr. Randolph Martin III
New England Research, Inc.
P.O. Box 857
Norwich, VT 05055

Dr. Gary McCartor
Mission Research Corp.
735 State Street
P.O. Drawer 719
Santa Barbara, CA 93102   (2 copies)

Professor Thomas V. McEvilly
Seismographic Station
University of California
Berkeley, CA 94720

Dr. Keith L. McLaughlin
Teledyne Geotech
314 Montgomery Street
Alexandria, VA 22314

Professor William Menke
Lamont-Doherty Geological Observatory
  of Columbia University
Palisades, NY 10964

Professor Brian J. Mitchell
Department of Earth & Atmospheric
      Sciences
Saint Louis University
Saint Louis, MO 63156

Mr. Jack Murphy
S-CUBED
A Division of Maxwell Laboratory
11800 Sunrise Valley Drive
Suite 1212
Reston, VA 22091 (2 copies)

Professor Otto W. Nuttli
Department of Earth &
 Atmospheric Sciences
Saint Louis University
Saint Louis, MO 63156

Professor J. A. Orcutt
Institute of Geophysics and Planetary
 Physics, A-205
Scripps Institute of Oceanography
Univ. of California, San Diego
La Jolla, CA 92093

Professor Keith Priestley
University of Nevada
Mackay School of Mines
Reno, Nevada 89557

Professor Charles G. Sammis
Center for Earth Sciences
University of Southern California
University Park
Los Angeles, CA 90089-0741

Dr. Jeffrey L. Stevens
S-CUBED,
A Division of Maxwell Laboratory
P.O. Box 1620
La Jolla, CA 92038-1620

Professor Brian Stump
Institute for the Study of Earth & Man
Geophysical Laboratory
Southern Methodist University
Dallas, TX 75275

Professor Ta-liang Teng
Center for Earth Sciences
University of Southern California
University Park
Los Angeles, CA 90089-0741

Professor M. Nafi Toksoz
Earth Resources Lab
Dept of Earth, Atmospheric and
 Planetary Sciences
Massachusetts Institute of Technology
42 Carleton Street
Cambridge, MA 02142

Professor Terry C. Wallace
Department of Geosciences
Building #11
University of Arizona
Tucson, AZ 85721

Professor Francis T. Wu
Department of Geological Sciences
State University of new York
  At Binghamton
Vestal, NY   13901

Dr. Monem Abdel-Gawad
Rockwell Internat'l Science Center
1049 Camino Dos Rios
Thousand Oaks, CA 91360

Professor Shelton S. Alexander
Geosciences Department
403 Deike Building
The Pennsylvania State University
University Park, PA 16802

Dr. Muawia Barazangi
Geological Sciences
Cornell University
Ithaca, NY 14853

Mr. William J. Best
907 Westwood Drive
Vienna, VA 22180

Dr. N. Biswas
Geophysical Institute
University of Alaska
Fairbanks, AK 99701

Dr. G. A. Bollinger
Department of Geological Sciences
Virginia Polytechnical Institute
21044 Derring Hall
Blacksburg, VA 24061

Dr. James Bulau
Rockwell Int'l Science Center
1049 Camino Dos Rios
P.O. Box 1085
Thousand Oaks, CA 91360

Mr. Roy Burger
1221 Serry Rd.
Schenectady, NY 12309

Dr. Robert Burridge
Schlumberger-Doll Resch Ctr.
Old Quarry Road
Ridgefield, CT 06877

Science Horizons, Inc.
ATTN: Dr. Theodore Cherry
710 Encinitas Blvd., Suite 101
Encinitas, CA 92024 (2 copies)

Professor Jon F. Claerbout
Professor Amos Nur
Dept. of Geophysics
Stanford University
Stanford, CA 94305 (2 copies)

Dr. Anton W. Dainty
AFGL/LWH
Hanscom AFB, MA 01731

Professor Adam Dziewonski
Hoffman Laboratory
Harvard University
20 Oxford St.
Cambridge, MA 02138

Professor John Ebel
Dept of Geology & Geophysics
Boston College
Chestnut Hill, MA 02167

Dr. Alexander Florence
SRI International
333 Ravenwood Avenue
Menlo Park, CA 94025-3493

Dr. Donald Forsyth
Dept. of Geological Sciences
Brown University
Providence, RI 02912

Dr. Anthony Gangi
Texas A&M University
Department of Geophysics
College Station, TX 77843

Dr. Freeman Gilbert
Institute of Geophysics &
  Planetary Physics
Univ. of California, San Diego
P.O. Box 109
La Jolla, CA 92037

Mr. Edward Giller
Pacific Seirra Research Corp.
1401 Wilson Boulevard
Arlington, VA 22209

Dr. Jeffrey W. Given
Sierra Geophysics
11255 Kirkland Way
Kirkland, WA 98033

Dr. Arthur Lerner-Lam
Lamont-Doherty Geological Observatory
 of Columbia University
Palisades, NY 10964

Dr. L. Timothy Long
School of Geophysical Sciences
Georgia Institute of Technology
Atlanta, GA 30332

Dr. George R. Mellman
Sierra Geophysics
11255 Kirkland Way
Kirkland, WA 98033

Dr. Bernard Minster
Institute of Geophysics and Planetary
   Physics, A-205
Scripps Institute of Oceanography
Univ. of California, San Diego
La Jolla, CA 92093

Dr. Geza Nagy
SRI International
333 Ravenswood Avenue
Menlo Park, CA 94025-3493

Dr. Jack Oliver
Department of Geology
Cornell University
Ithaca, NY 14850

Dr. Robert Phinney/Dr. F.A. Dahlen
Dept of Geological
   Geophysical Sci. University
Princeton University
Princeton, NJ 08540 (2 copies)

Professor Paul G. Richards
Lamont-Doherty Geological
 Observatory of Columbia Univ.
Palisades, NY 10964

Dr. Norton Rimer
S-CUBED
A Division of Maxwell Laboratory
P.O. 1620
La Jolla, CA 92038-1620

Professor Larry J. Ruff
Department of Geological Sciences
1006 C.C. Little Building
University of Michigan
Ann Arbor, MI 48109-1063

Dr. Alan S. Ryall, Jr.
Center of Seismic Studies
1300 North 17th Street
Suite 1450
Arlington, VA 22209-2308   (4 copies)

Dr. David G. Simpson
Lamont-Doherty Geological Observ.
 of Columbia University
Palisades, NY 10964

Dr. Bob Smith
Department of Geophysics
University of Utah
1400 East 2nd South
Salt Lake City, UT 84112

Dr. S. W. Smith
Geophysics Program
University of Washington
Seattle, WA 98195

Rondout Associates
ATTN: Dr. George Sutton,
Dr. Jerry Carter, Dr. Paul Pomeroy
P.O. Box 224
Stone Ridge, NY 12484 (4 copies)

Dr. L. Sykes
Lamont Doherty Geological Observ.
Columbia University
Palisades, NY 10964

Dr. Pradeep Talwani
Department of Geological Sciences
University of South Carolina
Columbia, SC 29208

Dr. R. B. Tittmann
Rockwell International Science Center
1049 Camino Dos Rios
P.O. Box 1085
Thousand Oaks, CA 91360

Weidlinger Associates
ATTN: Dr. Gregory Wojcik
620 Hansen Way, Suite 100
Palo Alto, CA 94304

Professor John H. Woodhouse
Hoffman Laboratory
Harvard University
20 Oxford St.
Cambridge, MA 02138

Dr. Gregory B. Young
ENSCO, Inc.
5400 Port Royal Road
Springfield, VA 22151-2388

Dr. Peter Basham
Earth Physics Branch
Geological Survey of Canada
1 Observatory Crescent
Ottawa, Ontario
CANADA K1A 0Y3

Dr. Eduard Berg
Institute of Geophysics
University of Hawaii
Honolulu, HI 96822

Dr. Michel Bouchon - Universite
  Scientifique et Medicale de Grenob
Lab de Geophysique - Interne et
  Tectonophysique - I.R.I.G.M-B.P.
38402 St. Martin D'Heres
Cedex FRANCE

Dr. Hilmar Bungum/NTNF/NORSAR
P.O. Box 51
Norwegian Council of Science,
Industry and Research, NORSAR
N-2007 Kjeller, NORWAY

Dr. Michel Campillo
I.R.I.G.M.-B.P. 68
38402 St. Martin D'Heres
Cedex, FRANCE

Dr. Kin-Yip Chun
Geophysics Division
Physics Department
University of Toronto
Ontario, CANADA M5S 1A7

Dr. Alan Douglas
Ministry of Defense
Blacknest, Brimpton,
 Reading RG7-4RS
UNITED KINGDOM

Dr. Manfred Henger
Fed. Inst. For Geosciences & Nat'l Res.
Postfach 510153
D-3000 Hannover 51
FEDERAL REPUBLIC OF GERMANY

Dr. E. Husebye
NTNF/NORSAR
P.O. Box 51
N-2007 Kjeller, NORWAY

NTNF/NORSAR
P.O. Box 51
N-2007 Kjeller, NORWAY

Mr. Peter Marshall, Procurement
 Executive, Ministry of Defense
Blacknest, Brimpton,
 Reading FG7-4RS
UNITED KINGDOM (3 copies)

Dr. Ben Menaheim
Weizman Institute of Science
Rehovot, ISRAEL 951729

Dr. Svein Mykkeltveit
NTNF/NORSAR
P.O. Box 51
N-2007 Kjeller, NORWAY (3 copies)

Dr. Robert North
Geophysics Division
Geological Survey of Canada
1 Observatory crescent
Ottawa, Ontario
CANADA, K1A OY3

Dr. Frode Ringdal
NTNF/NORSAR
P.O. Box 51
N-2007 Kjeller, NORWAY

Dr. Jorg Schlittenhardt
Federal Inst. for Geosciences & Nat'l Res.
Postfach 510153
D-3000 Hannover 51
FEDERAL REPUBLIC OF GERMANY

University of Hawaii
Institute of Geophysics
ATTN: Dr. Daniel Walker
Honolulu, HI 96822

Dr. Ramon Cabre, S.J.
c/o Mr. Ralph Buck
Economic Consular
American Embassy
APO Miami, Florida 34032

Professor Peter Harjes
Institute for Geophysik
Rhur University/Bochum
P.O. Box 102148, 4630 Bochum 1
FEDERAL REPUBLIC OF GERMANY

Professor Brian L.N. Kennett
Research School of Earth Sciences
Institute of Advanced Studies
G.P.O. Box 4
Canberra 2601
AUSTRALIA

Dr. B. Massinon
Societe Radiomana
27, Rue Claude Bernard
7,005, Paris, FRANCE (2 copies)

Dr. Pierre Mechler
Societe Radiomana
27, Rue Claude Bernard
75005, Paris, FRANCE

Dr. Ralph Alewine III
DARPA/NMRO
1400 Wilson Boulevard
Arlington, VA 22209-2308

Dr. Peter Basham
Geological Survey of Canada
1 Observatory Creseut
Ottowa, Ontario
CANADA K1A OY3

Dr. Robert Blandford
DARPA/NMRO
1400 Wilson Boulevard
Arlington, VA 22209-2308

Sandia National Laboratory
ATTN: Dr. H. B. Durham
Albuquerque, NM 87185

Dr. Jack Evernden
USGS-Earthquake Studies
345 Middlefield Road
Menlo Park, CA 94025

U.S. Geological Survey
ATTN: Dr. T. Hanks
Nat'l Earthquake Resch Center
345 Middlefield Road
Menlo Park, CA 94025

Dr. James Hannon
Lawrence Livermore Nat'l Lab.
P.O. Box 808
Livermore, CA 94550

U.S. Arms Control & Disarm. Agency
ATTN: Mrs. M. Hoinkes
Div. of Multilateral Affairs
Room 5499
Washington, D.C. 20451

Paul Johnson
ESS-4, Mail Stop J979
Los Alamos National Laboratory
Los Alamos, NM 87545

Ms. Ann Kerr
DARPA/NMRO
1400 Wilson Boulevard
Arlington, VA 22209-2308

Dr. Max Koontz
US Dept of Energy/DP 331
Forrestal Building
1000 Independence Ave.
Washington, D.C. 20585

Dr. W. H. K. Lee
USGS
Office of Earthquakes, Volcanoes,
  & Engineering
Branch of Seismology
345 Middlefield Rd
Menlo Park, CA 94025

Dr. William Leith
USGS
Mail Stop 928
Reston, VA 22092

Dr. Robert Masse'
Box 25046, Mail Stop 967
Denver Federal Center
Denver, Colorado 80225

Dr. Keith K. Nakanishi
Lawrence Livermore National Laboratory
P.O. Box 808, L-205
Livermore, CA 94550 (2 copies)

Dr. Carl Newton
Los Alamos National Lab.
P.O. Box 1663
Mail Stop C335, Group E553
Los Alamos, NM 87545

Dr. Kenneth H. Olsen
Los Alamos Scientific Lab.
Post Office Box 1663
Los Alamos, NM 87545

Howard J. Patton
Lawrence Livermore National Laboratory
P.O. Box 808, L-205
Livermore, CA 94550

HQ AFTAC/TG
Attn: Dr. Frank F. Pilotte
Patrick AFB, Florida 32925-6001

Mr. Jack Rachlin
USGS - Geology, Rm 3 C136
Mail Stop 928 National Center
Reston, VA 22092

Robert Reinke
AFWL/NTESG
Kirtland AFB, NM 87117-6008

HQ AFTAC/TGR
Attn: Dr. George H. Rothe
Patrick AFB, Florida 32925-6001

Donald L. Springer
Lawrence Livermore National Laboratory
P.O. Box 808, L-205
Livermore, CA 94550

Dr. Lawrence Turnbull
OSWR/NED
Central Intelligence Agency
CIA, Room 5G48
Washington, D.C. 20505

Dr. Thomas Weaver
Los Alamos Scientific Laboratory
Los Almos, NM 97544

AFGL/SULL
Research Library
Hanscom AFB, MA 01731-5000 (2 copies)

Secretary of the Air Force (SAFRD)
Washington, DC 20330
Office of the Secretary Defense
DDR & E
Washington, DC 20330

HQ DNA
ATTN: Technical Library
Washington, DC 20305

Director, Technical Information
DARPA
1400 Wilson Blvd.
Arlington, VA 22209

AFGL/XO
Hanscom AFB, MA 01731-5000

AFGL/LW
Hanscom AFB, MA 01731-5000

DARPA/PM
1400 Wilson Boulevard
Arlington, VA 22209

Defense Technical
Information Center
Cameron Station
Alexandria, VA 22314
(12 copies)

Defense Intelligence Agency
Directorate for Scientific &
Technical Intelligence
Washington, D.C. 20301

Defense Nuclear Agency/SPSS
ATTN: Dr. Michael Shore
6801 Telegraph Road
Alexandria, VA 22310

AFOSR/NPG
ATTN: Major John Prince
Bldg 410, Room C222
Bolling AFB, Wash D.C. 20332

AFTAC/CA (STINFO)
Patrick AFB, FL 32925-6001

END

DATE

FILMED

DTIC

4/88